

# Temporal refraction and reflection in modulated mechanical metabeams: theory and physical observation

Shaoyun Wang<sup>1,+</sup>, Nan Shao<sup>1,+</sup>, Hui Chen<sup>2</sup>, Jiaji Chen<sup>1</sup>, Honghua Qian<sup>1</sup>, Qian Wu<sup>1</sup>, Huiling Duan<sup>5</sup>, Andrea Alù<sup>3,4,\*</sup>, and Guoliang Huang<sup>5,\*</sup>

<sup>1</sup>Department of Mechanical and Aerospace Engineering, University of Missouri, Columbia, MO 65211, USA

<sup>2</sup>Center for Mechanics Plus under Extreme Environments, School of Mechanical Engineering and Mechanics, Ningbo University, Ningbo 315211, China

<sup>3</sup>Photonics Initiative, Advanced Science Research Center, City University of New York, New York, NY, USA

<sup>4</sup>Physics Program, Graduate Center, City University of New York, New York, NY, USA

<sup>5</sup>Department of Mechanics and Engineering Science, College of Engineering, Peking University, Beijing 100871, PR China

\*aalu@gc.cuny.edu, guohuang@pku.edu.cn, glhuang911@gmail.com

+these authors contributed equally to this work

## ABSTRACT

Wave reflection and refraction at a time interface follow different conservation laws compared to conventional scattering at a spatial interface. This study presents the experimental demonstration of refraction and reflection of flexural waves across a temporal boundary in a continuum-based mechanical metabeam, and unveils opportunities that emerge by tailoring temporal scattering phenomena for phononic applications. We observe these phenomena in an elastic beam attached to an array of piezoelectric patches that can vary in time the effective elastic properties of the beam. Frequency conversion and phase conjugation are observed upon a single temporal interface. These results are consistent with the temporal Snell's law and Fresnel equations for temporal interfaces. Further, we illustrate the manipulation of amplitude and frequency spectra of flexural wave temporal refraction and reflection through multi-stepped temporal interfaces. Finally, by implementing a smooth time variation of wave impedance, we numerically and experimentally demonstrate the capabilities of the temporal metabeam to realize waveform morphing and information coding. Our findings lay the foundation for developing time-mechanical metamaterials and time-phononic crystals, offering new avenues for advanced phonon manipulation in both wave amplitude and frequency.

## 1 Introduction

Wave propagation in time-varying media exhibits dynamics that are strikingly different from those in space-varying media<sup>1-3</sup>. The breaking of time translation symmetry allows energy exchange between the wave and the time-varying medium due to Noether's theorem<sup>4,5</sup>, leading to phenomena such as frequency manipulation<sup>6</sup>, wave amplification<sup>7</sup>, and self-emission<sup>8-10</sup>. Additionally, the Kramers–Kronig relations, grounded in the principle of causality in time-varying systems, enable these systems to surpass well-established fundamental performance limits, including the Bode-Fano limit, Rozanov bound, and Chu limit<sup>11-14</sup>.

Despite these differences, wave propagation in time-varying media and space-varying media share notable analogies. Space-time duality suggests that phenomena observed in spatially varying systems generally have analogous temporal versions, and vice versa<sup>15-17</sup>. In suddenly varying systems, phenomena analogous to wave scattering at spatial interfaces—such as reflection and refraction<sup>18-22</sup>, anti-reflection coatings<sup>23</sup>, total internal reflection<sup>24</sup>, Goos–Hänchen effect<sup>25,26</sup>, wave holography<sup>27</sup>, double slit diffraction<sup>28</sup>, and photon collisions<sup>29</sup>, can occur at temporal interfaces. Moreover, in periodic and disordered systems, temporal analogs such as time crystals<sup>30-32</sup>, disordered time-varying media<sup>33-35</sup>,  $k$ -band gaps<sup>36</sup>, the topology of  $k$ -bands and corresponding temporal interface modes<sup>37</sup>, and  $k$ -gap solitons and breathers<sup>38,39</sup>, have been developed. In slowly (adiabatically) varying systems, perfect state transitions such as controllable frequency shifts<sup>40-42</sup>, topological state pumping<sup>43,44</sup>, and non-Abelian braiding<sup>45,46</sup> have been achieved in both space-varying and time-varying systems.

Among these phenomena, wave refraction and reflection at temporal interfaces, are considered one of the most fundamental phenomena, at the foundations of time crystals, yet they are often challenging to achieve in practical wave systems. One of the key challenges is the creation of a temporal boundary, which typically requires a spatially uniform, ultrafast, and large change of

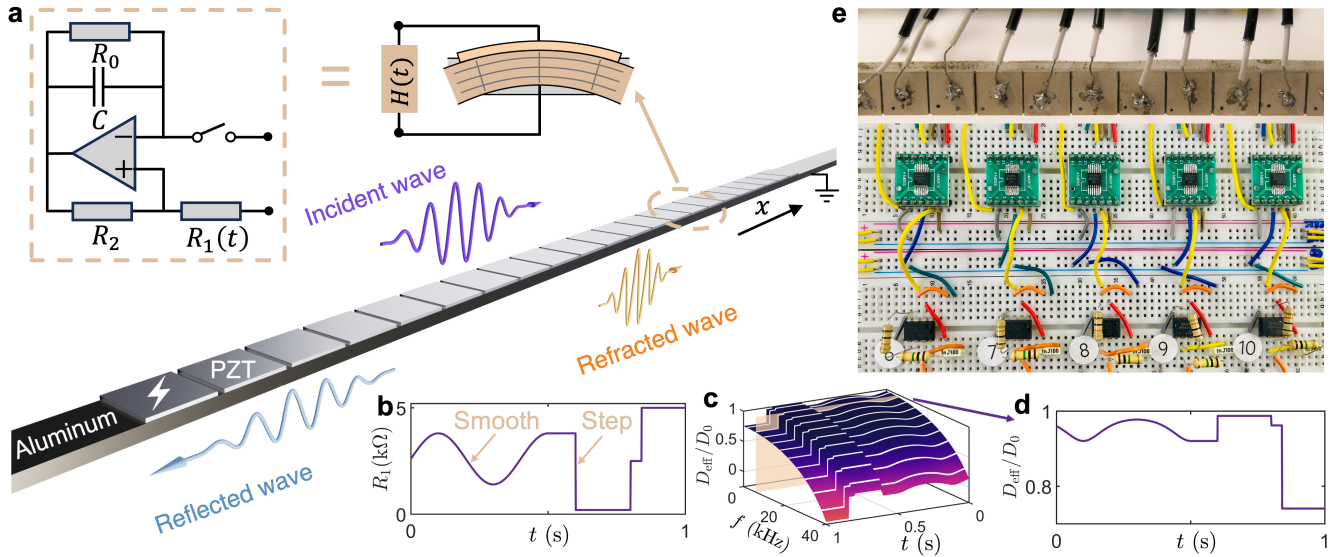


**Figure 1. Design of a time-varying metabeam.** **a** A segment of the time-varying metabeam designed to enable temporal scattering phenomena, such as temporal refraction and reflection, includes a unit cell equipped with a piezoelectric patch and voltage excitation (lightning sign), where the time-varying transfer function is implemented using an electric circuit network. **b** A plot illustrating a time-varying transfer function  $H(t)$ , which includes both smooth and step changes over time. **c** A graph showing the variation in effective bending stiffness as a function of both frequency  $f$  and time  $t$ , based on the time-varying transfer function  $H(t)$  from (b). Here, the bending stiffness  $D_0$  in open circuit status is  $0.88 \text{ N} \cdot \text{m}^2$ . **d** The effective bending stiffness  $D(t)$  plotted over time along the gray dashed line in (c), illustrating its time-dependent behavior. **e** Photo of the metabeam connected with time-varying electronic circuits labeled in each unit cell.

20 wave impedance<sup>19,47</sup>. The associated experimental challenges have kept the experimental study of wave scattering at temporal  
 21 interfaces in its infancy, particularly in the context of elastic media. Recently, the observation of temporal refraction and  
 22 reflection has been reported for electromagnetic waves leveraging transmission-line metamaterials<sup>19,21</sup>. A temporal phononic  
 23 interface consisting of discrete repelling magnets controlled by electromagnetic coils was also introduced to demonstrate the  
 24 temporal refraction of elastic waves<sup>48</sup>. However, a temporal interface in elastic continuum media, enabling temporal scattering  
 25 of flexural waves and the associated wave phenomena, has remained unexplored to date. Furthermore, wave scattering theory at  
 26 temporal interfaces has been mostly formulated within the framework of electromagnetics, leaving elastic counterparts, such as  
 27 Snell's law, Fresnel equations, and the principle of elastic momentum conservation, largely unexamined.

28 Elastic beams, equipped with piezoelectric patches connected to digital and analog circuits, provide an excellent platform  
 29 to achieve unconventional elastic wave phenomena, including the non-Hermitian skin effect<sup>49</sup>, odd mass density<sup>50</sup>, Willis  
 30 responses<sup>51</sup>, frequency conversion<sup>52</sup>, and topological pumping<sup>53</sup>. In this study, we demonstrate temporal interfaces for elastic  
 31 waves using the array of piezoelectric patches controlled by time-varying switching circuits that can produce a rapid, steplike  
 32 change in effective bending stiffness. The measured frequency conversion provides evidence of temporal refraction in a  
 33 continuum-based elastic system, and our developed theoretical model matches the experimental observation. By introducing  
 34 multiple temporal interfaces, we demonstrate further control over the manipulation of flexural waves in both amplitude and  
 35 frequency spectra. Finally, by programming a smooth time-varying transfer function to realize more adiabatic time interfaces,  
 36 we demonstrate additional capabilities in shaping the time-scattered waves in periodic and aperiodic fashion for smart waveform  
 37 morphing and information coding.

## 38 Results

### 39 A time-varying metabeam supporting temporal interfaces

40 The time-varying metamaterial under analysis consists of a long, thin beam where bending is the primary mode of deformation.  
 41 Each unit cell of this metabeam is equipped with a piezoelectric patch that senses bending deformation and provides a  
 42 self-response. The patch acts as a sensor by generating a voltage proportional to the elongation or contraction of the beam's  
 43 top surface (see Fig. 1a). The time-dependent transfer function,  $H(t)$ , comprises an analog switch, a microcontroller, and  
 44 a time-varying digital potentiometer  $R_1(t)$ , defined as  $H(t) = R_1(t)/(R_2C)$ <sup>54–56</sup>, as illustrated in Fig. 1b. As a result, the  
 45 piezoelectric patch also serves as a mechanical actuator, elongating and contracting in response to the applied voltage, and

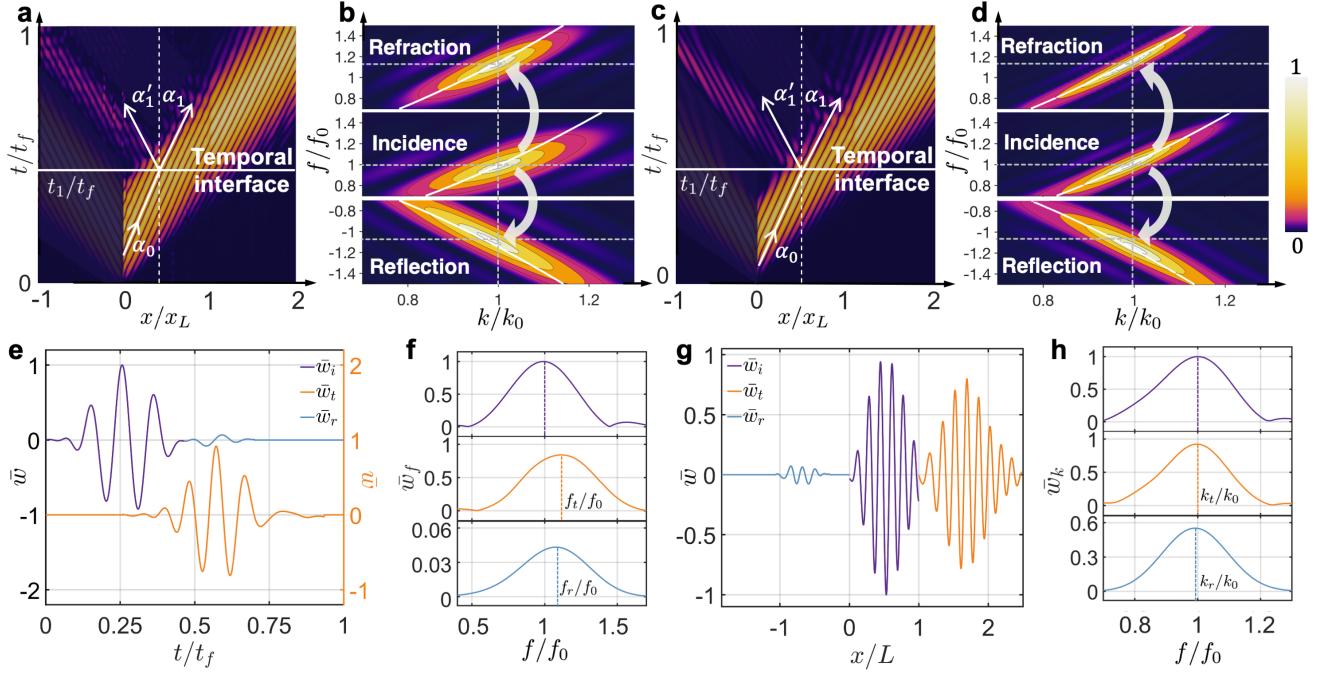


**Figure 2. Refraction and reflection of flexural waves at a temporal interface.** **a, c** The spacetime diagram of experimental (**a**) and simulated (**c**) wave scattering at a temporal interface  $t_1 = 0.44$  ms for an incident wave packet consisting of 3 cycles in the time domain with  $t_f = 1.1$  ms. The metabeam is positioned within the interval  $(0, L)$ , while the surrounding regions consist of an aluminum beam. The angles  $\alpha_i$ ,  $\alpha_1$ , and  $\alpha'_1$  represent the incident, refracted, and reflected angles, respectively. In **a**, these angles are  $49^\circ$ ,  $52^\circ$ , and  $52.5^\circ$ , while in **c**, they are  $47^\circ$ ,  $50.5^\circ$ , and  $51^\circ$ . **b, d** The top, middle, and bottom panels display the experimental (**b**) and simulated (**d**) contour diagrams of the refracted, incident, and reflected waves, respectively. The data is obtained from a 2D Fourier transformation of the experimental and simulated data shown in (**a**) and (**c**). The incident frequency  $f_0$  is 6.2 kHz and the incident wavenumber  $k_0$  is 119 rad/m. The white lines indicate dispersion curves from unit cell analysis. **e** The normalized incident ( $\bar{w}_i$ ) and reflected ( $\bar{w}_r$ ) signals measured at  $x/L = 0.05$ , along with the refracted signal ( $\bar{w}_t$ ) observed at  $x/L = 1$ . **f** Spectral analysis of the time-domain signals from (**e**). Here,  $f_0$ ,  $f_t$ , and  $f_r$  are the spectral peak frequencies of incident, refracted, and reflected waves, respectively. **g** The incident spatial profile ( $\bar{w}_i$ ) measured at  $t/t_f = 1/3$ , along with the refracted ( $\bar{w}_t$ ) and reflected ( $\bar{w}_r$ ) spatial profiles at  $t/t_f = 2/3$ . **h** Spectral analysis of the spatial-domain signals from (**g**). Here,  $k_0$ ,  $k_t$ , and  $k_r$  are the spectral peak wavenumbers of incident, refracted, and reflected waves, respectively.

46 thereby modifying the effective bending stiffness of the beam. To evaluate the performance of the metabeam, we numerically  
 47 calculated the time-varying effective bending stiffness using COMSOL simulations (see [Supplementary Section 1](#) for details).  
 48 The resultant effective time-varying bending stiffness of the metabeam  $D(t)$  across different frequencies and times can be  
 49 found in Fig. 1c. Specifically, Fig. 1d illustrates the effective bending stiffness as a function of time for a particular frequency,  
 50 intersected by the orange surface in Fig. 1c.

51 We conducted a thorough experimental investigation of the refraction and reflection of flexural waves at a temporal interface.  
 52 We employ a one-dimensional metabeam controlled by a time-varying electric circuit network as illustrated in Fig. 1e. The  
 53 temporal interface is created by toggling the analog switch between ON and OFF states. When the switch is ON,  $R_1$  is set to 5  
 54 k $\Omega$ , corresponding to a bending stiffness of  $0.63 \text{ N} \cdot \text{m}^2$ . When the switch is OFF,  $R_1$  becomes effectively infinite ( $\infty$ ), resulting  
 55 in a bending stiffness of  $0.88 \text{ N} \cdot \text{m}^2$ . In the experiment, a 3-cycle tone-burst signal with a central frequency of 6 kHz is applied at  
 56 the left interface ( $x/L = 0$ ) between the host beam and the modulated metabeam. Flexural wave fields are measured throughout  
 57 the system using a scanning laser Doppler vibrometer (Polytec PSV-400), as shown in Fig. 2a. At  $t_1/t_f = 0.44$ , the switch  
 58 transitions from ON to OFF, creating a step-change boundary that causes a rapid shift in the bending stiffness of the modulated  
 59 metabeam section. The switching time is 150 ns, ensuring an ideal temporal interface. Further details on the experimental setup  
 60 can be found in the Methods and [Supplementary Section 2](#). At the temporal interface, the incident wave splits into a temporally  
 61 right-propagating refracted wave and a temporally left-propagating reflected wave. In this figure, only the temporal reflection is  
 62 shown, with the left-propagating waves from incidence and spatial reflection at  $x/L = 1$  removed (see details in [Supplementary](#)  
 63 [Section 3](#)). We define the wavefront direction as the direction of wave propagation (see Fig. 2a,c). As such, the incident angle

(49° in the experiment and 47° in the simulation) differs from both the refracted angle (52° in the experiment and 50.5° in the simulation) and the reflected angle (52.5° in the experiment and 51° in the simulation), indicating a change in wave direction. The Fourier transform in Fig. 2b illustrates the frequency bandwidth of the input and output waves resulting from temporal reflection and refraction. It shows that the normalized frequency of the incident wave shifts from 1 to 1.16 for refraction and to 1.13 for reflection, while the normalized wavenumbers remain constant. Numerical simulations are performed to validate our experimental observations, as shown in Figs. 2c and 2d. The results exhibit excellent agreement between the measured output frequencies after the temporal boundary and the numerical predictions, both in the time and frequency domains. To further verify the frequency conversion and wavenumber invariance, time-domain signals measured at  $x/L = 0.05$  and  $x/L = 1$  are shown in Fig. 2e, where three distinct wave packets corresponding to the incident, refracted, and reflected waves are clearly visible. The normalized frequency  $f_i/f_0 = 1.15$  for the refracted wave and  $f_r/f_0 = 1.11$  for the reflected wave quantitatively demonstrate the shift relative to the input frequency of the incident wave, as shown in Fig. 2f, indicating a breakdown of energy conservation. Additionally, the spatial-domain signals measured at  $t/t_f = 1/3$  and  $t/t_f = 2/3$  are shown in Fig. 2g. The wavenumbers  $k_i$  for the refracted wave and  $k_r$  for the reflected wave are consistent with the wavenumber  $k_0$  of the incident wave, as depicted in Fig. 2h, demonstrating the conservation of momentum. The corresponding numerical results for Fig. 2e-h are provided in Supplementary Section 4. Further results on wave refraction and reflection during the switch from OFF to ON at different frequencies are provided in Supplementary Sections 5 and 6. The effect of finite switching time on wave refraction and reflection is discussed in Supplementary Section 7. To rule out spatial reflection, we simulate an asymmetric pair of wave packets, resulting in a reversed order of the reflected waves (see Supplementary Section 8 for details).

## Refraction and reflection of the flexural wave at a temporal interface

To understand frequency conversion through a temporal interface, we theoretically analyze flexural wave scattering at a temporal interface. In the absence of external forces, the behavior of flexural waves is governed by the Euler-Bernoulli beam equation with time-dependent bending stiffness, expressed as:

$$\frac{\partial}{\partial t} \left( \rho A \frac{\partial w(x,t)}{\partial t} \right) + \frac{\partial^2}{\partial x^2} \left( D(t) \frac{\partial^2 w(x,t)}{\partial x^2} \right) = 0, \quad (1)$$

where  $D = EI$  represents the bending stiffness,  $E$  is Young's modulus, and  $I$  is the second moment of area. Additionally,  $\rho$  denotes the density, and  $A$  represents the beam's cross-sectional area. For temporal refraction and reflection, the bending stiffness is modulated as a step function over time:  $D(t) = D_0 + (D_1 - D_0)\Theta(t - t_1)$ , where  $\Theta(t)$  is the Heaviside step function,  $D_0$  represents the initial bending stiffness, and  $D_1$  denotes the bending stiffness after an abrupt change at time  $t = t_1$ . The conditions for temporal continuity, outlined in Supplementary Section 9, guarantee the smooth transition of both momentum and displacement at the temporal interface without external forces. These conditions are formulated as follows:

$$\rho A \frac{\partial w}{\partial t} \Big|_{t=t_1^+} = \rho A \frac{\partial w}{\partial t} \Big|_{t=t_1^-}, \quad w \Big|_{t=t_1^+} = w \Big|_{t=t_1^-}. \quad (2)$$

Here, continuity conditions are applied to momentum and displacement fields, in analogy to the continuity of electric displacement  $\mathbf{D}$  and magnetic flux density  $\mathbf{B}$  in electrodynamics<sup>2</sup>. In our system, the absence of impulses ensures the continuity of momentum. Meanwhile, the invariance of density leads to the continuity of the velocity field, which, in turn, ensures the continuity of the displacement field.

The bending stiffness in Eq. (1) is constant in time at all instances, except at the time interface. Therefore, the wave obeys the conventional expressions stemming from the separation of variables both before and after the time interface. For medium 1 ( $t < t_1$ ), the solution for the incident wave, based on Eq. (1), can be expressed as:

$$w = A_i e^{ik_0 x - i\omega_0 t}, \quad t < t_1, \quad (3)$$

where  $A_i$  is the incident wave coefficient, and the angular frequency  $\omega_0$  and wavenumber  $k_0$  before the switching event satisfy the dispersion relation  $\omega_0 = \sqrt{D_0/(\rho A)} k_0^2$ . For medium 2 ( $t > t_1$ ), the displacement field, composed of the refracted and reflected waves after the switching event, can be expressed as:

$$w = \left[ T e^{-i\omega_1(t-t_1)} + R e^{i\omega_1(t-t_1)} \right] A_i e^{i(k_1 x - \omega_0 t_1)}, \quad t > t_1, \quad (4)$$

where  $T$  is the refraction coefficient, and  $R$  is the reflection coefficient. The angular frequency  $\omega_1$  and wavenumber  $k_1$  after the switching event are related by the equation  $\omega_1 = \sqrt{D_1/(\rho A)} k_1^2$ . By inserting the wave solutions from Eqs. (3) and (4) into the temporal continuity conditions given by Eq. (2), we obtain

$$\begin{aligned} e^{ik_0 x} &= (T + R) e^{ik_1 x}, \\ -i\omega_0 e^{ik_0 x} &= (-i\omega_1 T + i\omega_1 R) e^{ik_1 x}. \end{aligned} \quad (5)$$

105 The temporal continuity conditions in Eq. (5) satisfied at every point in space requires

$$k_1 = k_0, \quad (6)$$

106 or equivalently

$$\omega_1 n_1 = \omega_0 n_0, \quad (7)$$

107 where the elastic index of refraction is defined as  $n_j = \sqrt{\rho A / D_j}$ , with  $j = 0, 1$  representing the different media before and after  
 108 the switching event. Eq. (7) can be interpreted as the temporal Snell's law. Given the frequency of the incident wave and the  
 109 refractive indices before and after the switching event, the frequency of the refracted wave can be predicted using Eq. (7). The  
 110 more familiar form, which describes the geometric relationship between the angles of the incident and refracted waves in a  
 111 space-time diagram, is given by

$$\frac{\tan \alpha_1}{\tan \alpha_0} = \frac{n_0}{n_1}, \quad (8)$$

112 where  $\alpha_0$  is the incident angle and  $\alpha_1$  is the refracted angle. See [Supplementary Section 10](#) for the detailed derivation.

113 By substituting Eq. (6) and Eq. (7) into Eq. (5), we can obtain the temporal scattering coefficients as

$$R = \frac{1}{2} \left( 1 - \frac{Z_0}{Z_1} \right), \quad T = \frac{1}{2} \left( 1 + \frac{Z_0}{Z_1} \right), \quad (9)$$

114 where  $Z_j = \sqrt{\rho A D_j}$  with  $j = 0, 1$  represents the elastic impedance. Eq. (9) serves as the analog of Fresnel equations  
 115 at the temporal interface, predicting the amplitudes of the refracted and reflected waves. At the temporal interface, time-  
 116 translation invariance is broken, leading to a breakdown of energy conservation according to Noether's theorem (as detailed in  
 117 [Supplementary Section 11](#)). However, the system preserves space-translation invariance, ensuring that momentum is conserved.  
 118 This conserved momentum, also known as Noether's charge, of the elastic beam is given by

$$P = \int \rho A \left[ (\partial_t w)^\dagger \partial_x w + \partial_t w (\partial_x w)^\dagger \right] dx, \quad (10)$$

119 where  $\dagger$  denotes the Hermitian conjugate. The detailed derivation of Eq. (10) using the complex scalar field theory of the  
 120 Euler-Bernoulli beam is provided in [Supplementary Section 11](#). The momentum of the wave before the time switching is

$$P_0 = 2\rho A \omega_0 k_0 A_i^2, \quad (11)$$

121 whereas the momentum of the waves after the switching time is

$$P_1 = 2\rho A \omega_1 k_0 (T^2 - R^2) A_i^2. \quad (12)$$

122 With the aid of Eq. (9), the conservation of momentum can be easily verified as

$$P_0 = P_1 = 2Z_0 k_0^3 A_i^2. \quad (13)$$

123 In addition, the momentum of both the incident and scattered waves is proportional to  $k_0^3$ , indicating that the wavenumber  
 124 remains invariant.

125 Guided by the derived Snell's law in Eq. (7), the frequency conversion capability for different incident frequencies at the  
 126 temporal interface is further tested experimentally. Fig. 3a presents the measured central frequencies of the refracted (crosses)  
 127 and reflected (circles) waves at the temporal interface as a function of the incident frequency  $f_0$  (squares), for both the switch  
 128 from ON to OFF (top panel) and OFF to ON (bottom panel). In the figure, the corresponding time-domain signals are measured  
 129 at  $x/L = 0.05$  for the incident and reflected waves, and at  $x/L = 1$  for the refracted wave. The frequencies of the refracted and  
 130 reflected waves shift upward (downward) during the transition from ON to OFF (OFF to ON), confirming the occurrence of  
 131 frequency conversion. Furthermore, the frequencies of the refracted and reflected waves, normalized by the frequency of the  
 132 incident wave, are presented in Fig. 3b. Additionally, Fig. 3c presents the tangents of the angles for the incident, refracted,  
 133 and reflected waves, with the corresponding angles provided in [Supplementary Table 3](#). The discrepancy observed for the  
 134 switch from ON to OFF at 6 kHz arises because low-frequency incident signals do not terminate before reaching the temporal  
 135 boundary, while the discrepancy at high frequencies is attributed to the limitations of the homogeneous beam model at short  
 136 wavelengths. Overall, these normalized frequencies and tangent ratios agree with the theoretical predictions ( $n_0/n_1 = 1.17$  in  
 137 the top panel and  $n_0/n_1 = 0.85$  in the bottom panel) derived from Snell's law in Eq. (7) and Eq. (8). This agreement confirms

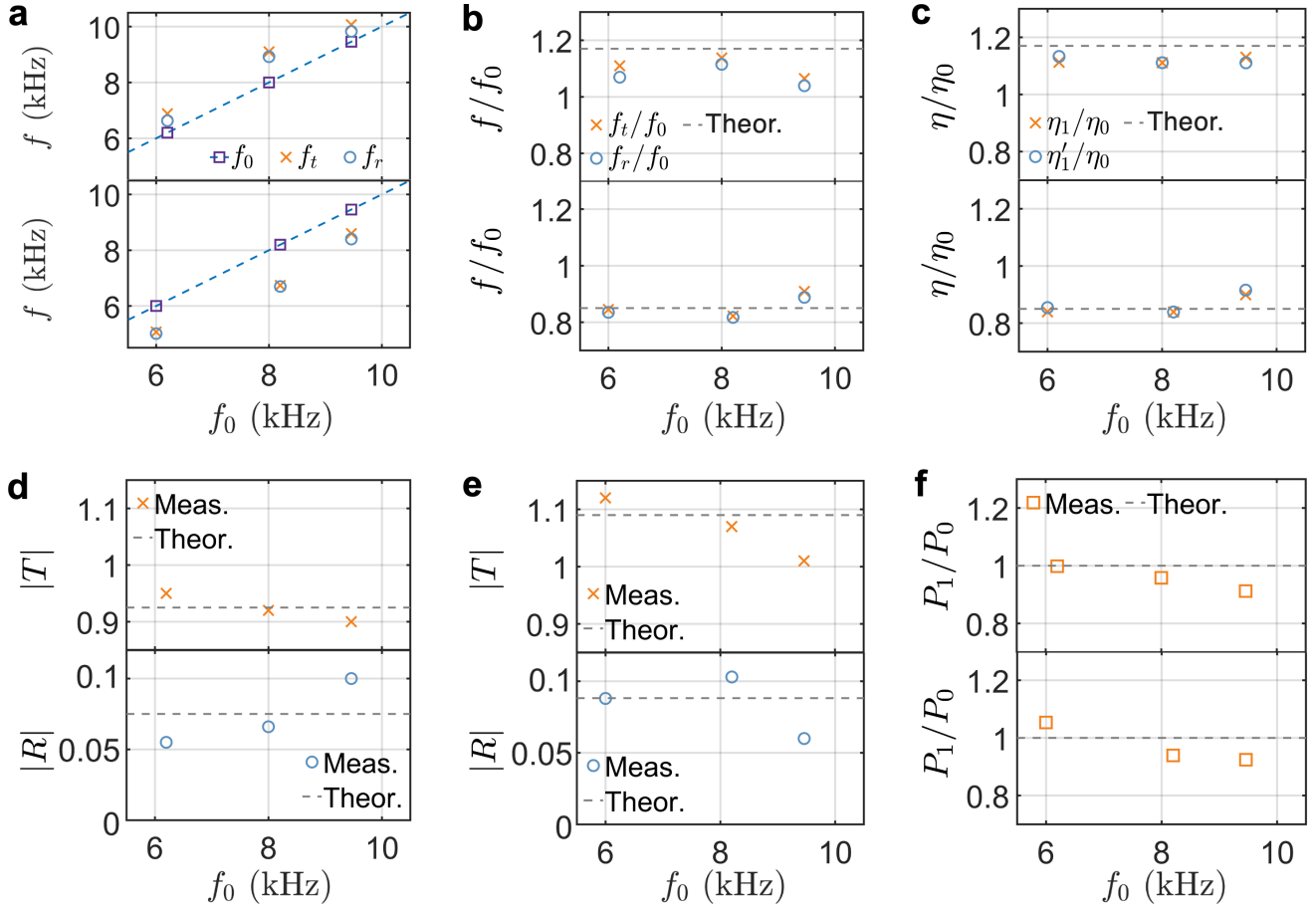


**Figure 3. Verification of temporal Snell's law, Fresnel equations, and momentum conservation.** **a** The measured frequencies of the incident (squares) and reflected (circles) signals at  $x/L = 0.05$ , and the refracted signal (crosses) observed at  $x/L = 1$ , plotted against the incident frequency  $f_0$ . The top (bottom) panel represents the results for the switch from ON to OFF (from OFF to ON). **b** Normalized frequencies of the refracted and reflected waves, along with the theoretical prediction of Snell's law (dashed line). The top (bottom) panel represents the results for the switch from ON to OFF (from OFF to ON). **c** The measured ratio of the tangent of the refraction angle ( $\eta_1 = \tan \alpha_1$ ) to the tangent of the incidence angle ( $\eta_0 = \tan \alpha_0$ ), along with the measured ratio of the tangent of the reflection angle ( $\eta'_1 = \tan \alpha'_1$ ) to the tangent of the incidence angle, is compared with the theoretical prediction based on Snell's law (represented by the dashed line). The top (bottom) panel represents the results for the switch from ON to OFF (from OFF to ON). **d** The measured and theoretical magnitudes of the refraction coefficient (top panel) and reflection coefficient (bottom panel) at  $t/t_f = 2/3$  for the switch from ON to OFF, plotted against the incident frequency  $f_0$ . **e** The measured and theoretical magnitudes of the refraction coefficient (top panel) and reflection coefficient (bottom panel) at  $t/t_f = 2/3$  for the switch from OFF to ON, plotted against the incident frequency  $f_0$ . **f** The ratio of momentum before and after the temporal interface, along with the theoretical prediction based on momentum conservation (shown as the dashed line). The top panel shows the results for the switch from ON to OFF, while the bottom panel corresponds to the switch from OFF to ON.

138 that the observed frequency conversion and directional changes are consistent with the analytical predictions based on the  
 139 temporal analog of Snell's law.

140 The derived Fresnel equations in Eq. (9) across the temporal boundary are also verified. The amplitudes of the incident,  
 141 refracted, and reflected waves are defined as the height of spectral peaks, as shown in Fig. 2h. The corresponding spatial-domain  
 142 signals are measured at  $t/t_f = 1/3$  for the incident wave, and at  $t/t_f = 2/3$  for the refracted and reflected waves. Figs. 3d,e  
 143 show the measured amplitudes of the refraction coefficient ( $T$ , crosses), reflection coefficient ( $R$ , circles), and their theoretical  
 144 predictions (dashed lines) based on Eq. (9), as functions of the incident frequency for the switches from ON to OFF and  
 145 OFF to ON, respectively. In Fig. 3d, the measured amplitudes closely match the theoretical predictions of  $|T| = 0.925$  and  
 146  $|R| = 0.075$  for the switch from ON to OFF at the given incident frequencies. Similarly, the minor deviation between the  
 147 experimental measurement and theoretical predictions may be attributed to the missing of the low-frequency incident signals  
 148 and the limitations of the homogeneous beam model. Also as shown in Fig. 3e, the measured amplitudes are mainly consistent  
 149 with the theoretical predictions of  $|T| = 1.09$  and  $|R| = 0.089$  for switching OFF to ON at different incident frequencies. A  
 150 small deviation is also observed. However, the reasonable consistency verifies the elastic analog of Fresnel equations across  
 151 various incident frequencies. Finally, the ratio of momentum before and after the temporal interface is presented in Fig. 3f.  
 152 The momentum ratios are mainly close to 1 for both the switch from ON to OFF and from OFF to ON, validating momentum  
 153 conservation.

### 154 Flexural wave engineering with temporal multi-stepped interfaces

155 Leveraging scattering phenomena at a single temporal interface, we explore the engineering of flexural wave interferences in  
 156 time, inspired by their photonic counterparts, such as in discrete temporal crystals and temporal metabeams analogous to the  
 157 optical counterpart<sup>23,57,58</sup>. To demonstrate this, we consider flexural wave propagation through a temporal modulation of the  
 158 bending stiffness characterized by  $M + 1$  stepped temporal interfaces, as depicted in Fig. 4a. The unbounded medium initially  
 159 has a refractive index  $n_0$  for times  $t < t_1$ . At  $t = t_1$ , a temporal modulation of the refractive index occurs, characterized by  
 160  $n_m$ ,  $m = 1, 2, \dots, M$  over  $M$  intervals. This assumption of step temporal transitions is highly idealized, as it implies an infinitely  
 161 fast response of the medium to the modulation. The theory of wave propagation through multi-stepped temporal interfaces in  
 162 an unbounded medium is developed using the rigorous transfer matrix approach. The wave components on the left and right  
 163 sides of the  $m$ th temporal slab are represented by  $[w_m^+, w_m^-]^T$  and  $[\tilde{w}_m^+, \tilde{w}_m^-]^T$ , respectively. These components are connected by  
 164 the following expression:

$$\begin{bmatrix} \tilde{w}_m^+ \\ \tilde{w}_m^- \end{bmatrix} = \mathbf{N}_a^m \begin{bmatrix} w_m^+ \\ w_m^- \end{bmatrix}, \quad (14)$$

165 where the propagation matrix  $\mathbf{N}_a^m$  is

$$\mathbf{N}_a^m = \begin{bmatrix} e^{-i\omega_m \Delta t_m} & 0 \\ 0 & e^{i\omega_m \Delta t_m} \end{bmatrix}, \quad (15)$$

166 and the  $m$ th time interval is  $\Delta t_m = t_{m+1} - t_m$ . In addition, due to the continuity equations in Eq. (2), the wave components  
 167  $[w_m^+, w_m^-]^T$  and  $[\tilde{w}_{m-1}^+, \tilde{w}_{m-1}^-]^T$  on either side of  $m$ th temporal interface satisfy the following relation:

$$\begin{bmatrix} w_m^+ \\ w_m^- \end{bmatrix} = \mathbf{N}_b^m \begin{bmatrix} \tilde{w}_{m-1}^+ \\ \tilde{w}_{m-1}^- \end{bmatrix}. \quad (16)$$

168 Here, the matching matrix  $\mathbf{N}_b^m$  is

$$\mathbf{N}_b^m = \begin{bmatrix} T_m & R_m \\ R_m & T_m \end{bmatrix}. \quad (17)$$

169 where  $T_m = 1 + Z_{m-1}/Z_m$  and  $R_m = 1 - Z_{m-1}/Z_m$ . Applying Eqs. (14) and (16) recurrently, we obtain the relationship between  
 170 the waves in the initial and final temporal boundaries:

$$\begin{bmatrix} w_{M+1}^+ \\ w_{M+1}^- \end{bmatrix} = \mathbf{N} \begin{bmatrix} w_0^+ \\ 0 \end{bmatrix}, \quad (18)$$

171 where the overall transfer matrix  $\mathbf{N}$  is given as follows:

$$\mathbf{N}(n, t, f_0) = \mathbf{N}_b^{M+1} \prod_{m=1}^M \mathbf{N}_a^m \mathbf{N}_b^m. \quad (19)$$

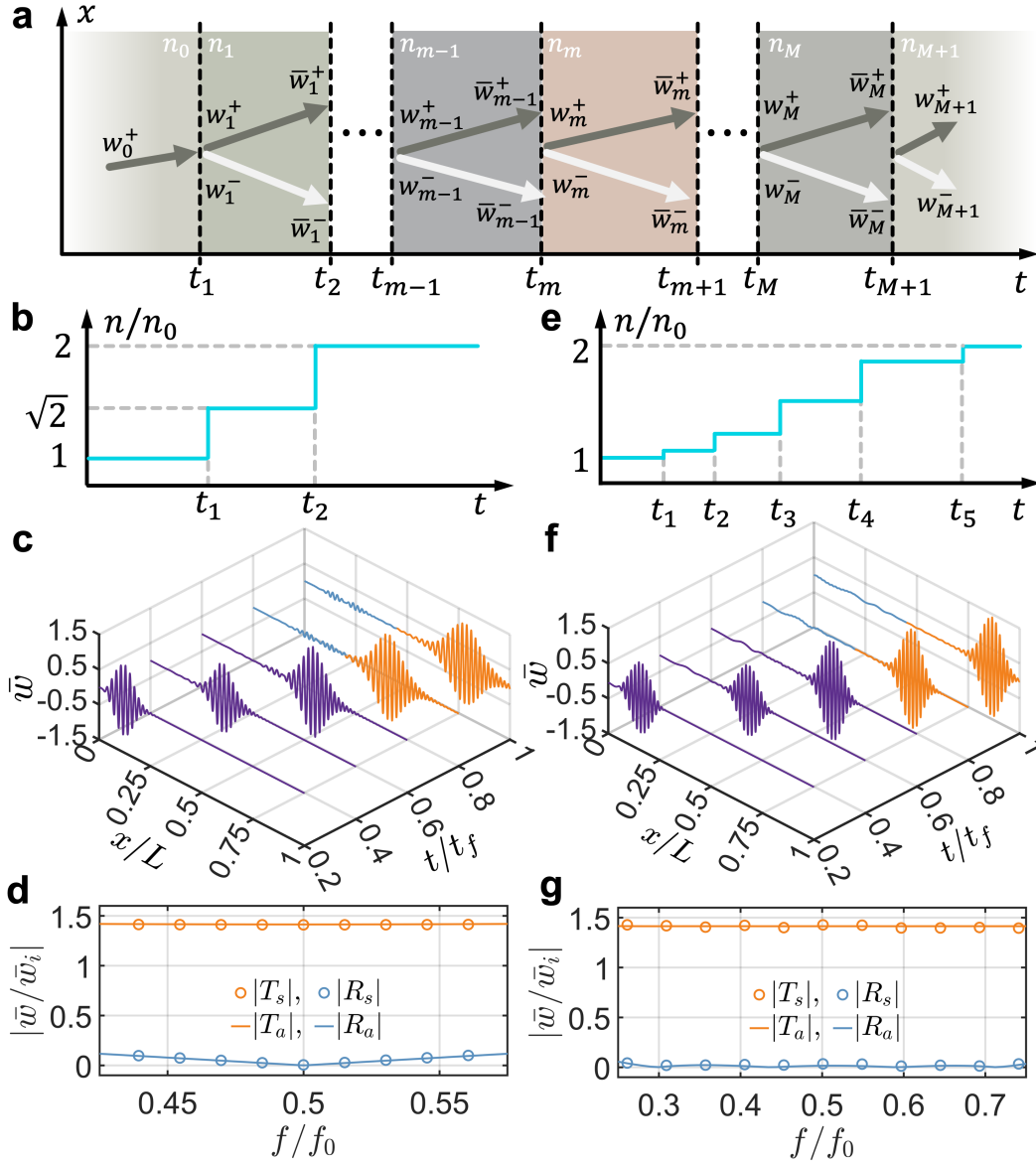


**Figure 4. Multi-stepped temporal interfaces for anti-reflection.** **a** Schematic diagram illustrating a wave propagating through multi-stepped temporal interfaces. The setup consists of two temporally semi-infinite media with a cascade of  $M$  temporal slabs, separated by  $M + 1$  temporal interfaces. **b, e** The optimal time-dependent index of refraction function designed for anti-reflection of a single frequency (**b**) and broadband frequency (**e**). **c, f** Wave packet evolution by COMSOL simulation for verifying anti-reflection of a single frequency (**c**) and broadband frequency (**f**). The wave packet, with a central frequency of 6 kHz, consists of 5 cycles in time, with  $t_f = 6$  ms and  $L = 2.56$  m. **d, g** Refraction and reflection coefficients as a function of the normalized incident frequency  $f/f_0$  for single frequency (**d**) and broadband frequency (**g**) anti-elimination, where  $f_0 = 6$  kHz, with circles representing numerical simulation results and solid lines representing analytical calculations using the transfer matrix method. The subscripts "s" and "a" denote simulated and analytical results, respectively. The results are obtained from the Fourier transform at  $t/t_f = 0.75$  in (**c**) and (**f**).



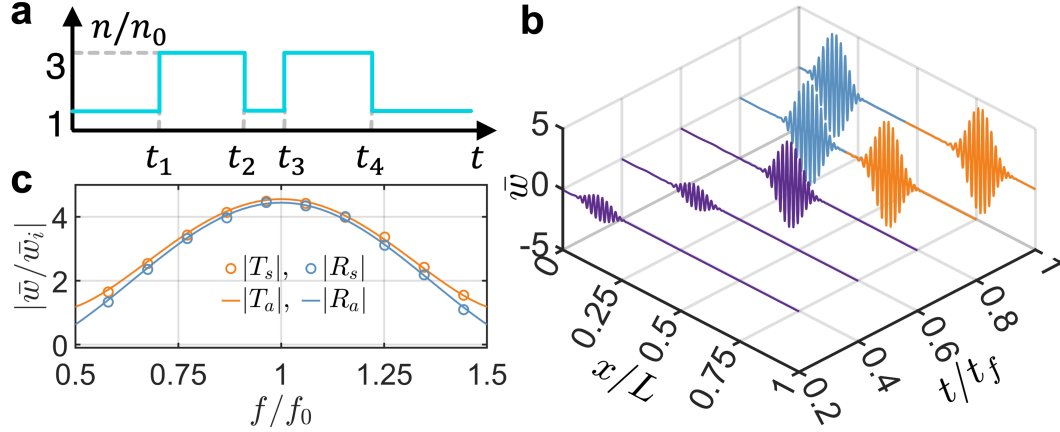


**Figure 5. Multi-stepped temporal interfaces for wave amplification.** **a** The optimal distribution of index of refraction with 4 temporal interfaces for wave amplification. **b** The evolution of the wave packet is simulated using COMSOL to verify wave amplification. This wave packet, with a central frequency of 6 kHz, consists of 5 cycles for  $t_f = 6$  ms and spans a length of  $L = 2.56$  m. **c** Refraction and reflection coefficients as a function of the normalized incident frequency  $f/f_0$ , where  $f_0 = 6$  kHz, with circles representing numerical simulation results and solid lines representing analytical calculations using the transfer matrix method. The subscripts "s" and "a" denote simulated and analytical results, respectively. The results are obtained from the Fourier transform of data at  $t/t_f = 0.75$  in (b)

172 Here,  $n$  and  $t$  are vectors representing the refractive indices  $n_m$  (for  $m = 1, 2, \dots, M$ ) and the times at different interfaces  $t_m$  (for  
 173  $m = 1, 2, \dots, M + 1$ ), respectively.  $f_0$  denotes the wave frequency in the left unbounded medium. Additionally, the refraction  
 174 coefficient is defined as  $T(n, t, f_0) = w_{M+1}^+ / w_0^+ = N_{11}$ , and the reflection coefficient is defined as  $R(n, t, f_0) = w_{M+1}^- / w_0^+ = N_{21}$ .

175 Using the analytical solutions for the reflection and refraction coefficients, we will explore three examples of engineered  
 176 flexural wave propagation across multi-stepped temporal interfaces through inverse design. These examples will leverage  
 177 temporal intervals and modulated slab parameters, demonstrating the potential of temporal multi-stepped interfaces as versatile  
 178 wave transformers. First, we investigate anti-reflection temporal coatings by introducing two-stepped temporal slabs with  
 179 equal travel times to achieve impedance matching and frequency conversion between two connected waveguides with different  
 180 stiffnesses, analogous to quarter-wavelength impedance matching in the spatial domain<sup>59</sup>. Second, we employ multi-stepped  
 181 temporal interfaces composed of five temporal slabs to achieve broadband wave anti-reflection<sup>57</sup>. Finally, we propose temporal  
 182 multi-stepped interfaces with alternating high and low refractive indices to enable wave amplification in both reflection and  
 183 refraction<sup>58</sup>. The temporal parameters of these multi-stepped structures are determined using an optimization method, which  
 184 seeks to identify the optimal temporal interface parameters by minimizing a target function related to the reflection and  
 185 refraction coefficients, subject to specified constraints. Detailed formulations of the optimization problem for the three cases  
 186 are provided in [Supplementary Section 12](#), and the optimized results will be validated against the analytical solution from Eq.  
 187 (19) for multi-stepped interfaces using the optimized parameters.

188 Fig. 4b presents the numerically derived two-stepped temporal configuration, consisting of a single temporal slab with  
 189 a refractive index  $n_1$ , designed to eliminate the reflection of an incident flexural wave at a frequency of  $f_0 = 6$  kHz, closely  
 190 matching our experimental testing conditions. The duration of the temporal slab is defined as  $\Delta t_1 = t_2 - t_1$ . The wave initially  
 191 propagates through a medium with a refractive index of  $n_0$ , while the final medium has a refractive index of  $n_2 = 2n_0$ . By  
 192 minimizing the square of the reflection coefficient magnitude at the frequency (see [Supplementary Section 12](#) for details), we  
 193 obtain the optimal values of  $n_1 = 1.414n_0$  and  $\Delta t_1 = 0.3536/f_0$ . These results are in excellent agreement with the analytical  
 194 solution in Eq. (18), where  $n_1 = \sqrt{2}n_0$  and  $t_2 = 1/(2\sqrt{2}f_0)$  (see Methods)<sup>23</sup>. Since the time duration  $t_2$  equals a quarter of the  
 195 wave period in the slab, this temporal medium is referred to as a quarter-wave transformer. Physically, as the incident wave  
 196 passes through two temporal interfaces, it generates two refracted and two reflected waves. In the quarter-wave transformer,  
 197 the two reflected waves cancel each other through coherent subtraction. Using the optimized parameters, Fig. 4c illustrates  
 198 the evolution of a wave packet with a central frequency of  $f_0 = 6$  kHz as it propagates through the temporal quarter-wave  
 199 transformer. The simulation is performed in a long temporal metabeam with 240 unit cells (see [Supplementary Section 4](#)  
 200 for details on refraction and reflection without the temporal slab). In Fig. 4c, the reflected wave packet is almost entirely  
 201 suppressed, though two small wave packets with different frequencies are generated. This occurs because the transformer  
 202 perfectly eliminates reflection at the frequency, while residual components remain at other frequencies<sup>23</sup>. Additional simulations  
 203 were performed for wave packets with different central frequencies, and the corresponding refraction coefficient  $T_s$  and reflection

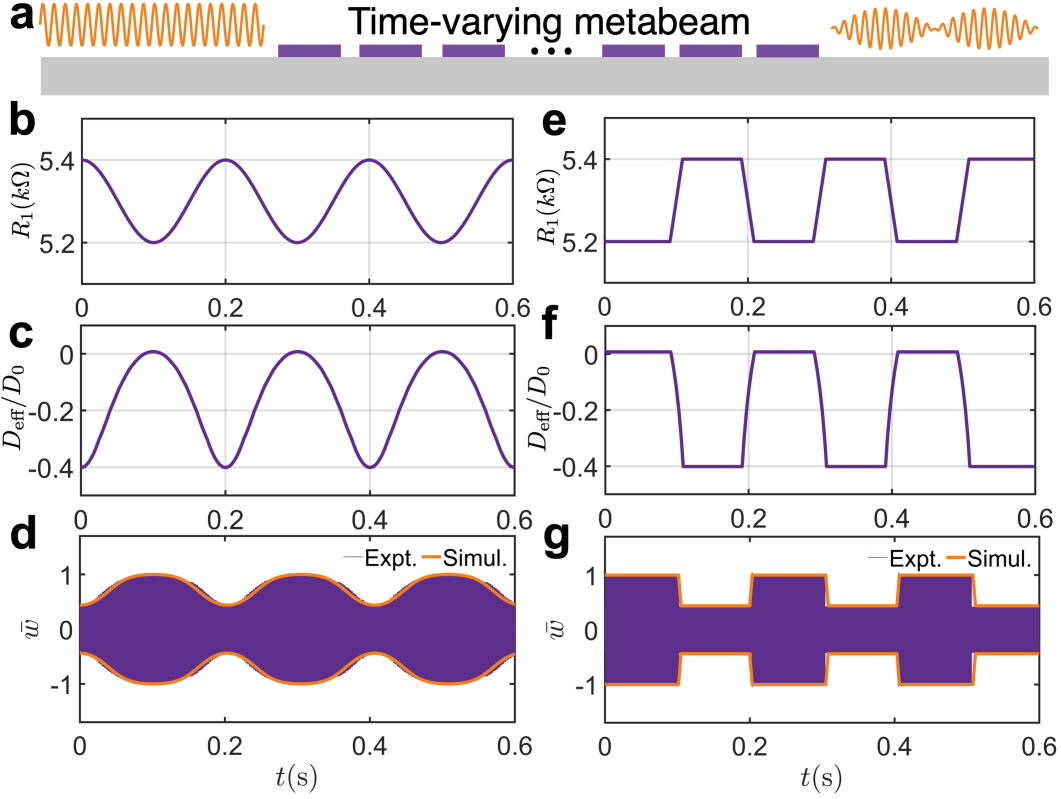


**Figure 6. Smart waveform morphing schematic enabled by a smooth time-varying metabeam.** **a** Schematic illustration of smart waveform morphing enabled by a time-varying metabeam. **b, e** The transfer function can be modulated into various forms, such as a sinusoidal function (**b**) and smooth step function (**e**). **c, f** The corresponding effective bending stiffness over time at frequencies of 33 kHz of sinusoidal function and smooth step function, respectively. **d, g** The simulated response (encapsulated by an orange envelope) and the measured time response (purple lines) at a point on the right side of the beam of the sinusoidal function and smooth step function, respectively. The excitation source, with a frequency of 33 kHz, is located at the leftmost piezoelectric patch.

204 coefficient  $R_s$  are plotted in Fig. 4d. In this figure, the numerical refraction coefficient  $T_s$  and reflection coefficient  $R_s$  (circles)  
 205 closely match the analytical refraction coefficient  $T_a$  and reflection coefficient  $R_a$  (solid lines), calculated using the transfer  
 206 matrix method. The reflection coefficient approaches zero near  $0.5f_0$  but diverges significantly at other frequencies, confirming  
 207 that the temporal quarter-wave transformer eliminates reflection optimally and shifts the frequency component to the frequency  
 208  $0.5f_0$ . The magnitude of the frequency shift is determined by the refractive index change through the temporal interfaces. It is  
 209 also observed that the values of scattering coefficient  $T_s$  are greater than unity for most frequencies, revealing a gain effect  
 210 induced on the propagating signal by the medium, where energy conservation is violated.

211 To achieve broadband wave anti-reflection, the multi-stepped interfaces are determined using an optimization method.  
 212 Fig. 4e shows the resulting temporal medium with four slabs, characterized by  $n = [1.075, 1.271, 1.573, 1.860]n_0$  and  $t =$   
 213  $[0, 0.262, 0.575, 0.962, 1.416]/f_0$ , designed for broadband anti-reflection across the frequency range from  $0.5f_0$  to  $1.5f_0$ . The  
 214 initial and final refractive indices are  $n_0$  and  $n_2 = 2n_0$ , respectively. These parameters are derived by minimizing the integral  
 215 of the squared reflection coefficient over the same frequency range (see [Supplementary Section 12](#) for details). The wave  
 216 packet evolution in this medium is shown in Fig. 4f, where reflections are significantly suppressed, except for minor low-  
 217 and high-frequency noise. Fig. 4g shows the simulated and analytical refraction and reflection coefficients in the frequency  
 218 domain, with the simulated reflection coefficient staying near zero across the range from  $0.25f_0$  to  $0.75f_0$ , where the frequency  
 219 shifts relative to the incident frequency. This result is consistent with the analytical results from the transfer matrix method,  
 220 confirming the accuracy of the optimization method and the effectiveness of temporal multi-stepped interfaces for broadband  
 221 anti-reflection.

222 Different from spatial interfaces, time interfaces can provide energy to the input waves, hence through interference it is  
 223 possible to design time scattering profiles that achieve broadband wave amplification in both reflected and refracted waves. Fig.

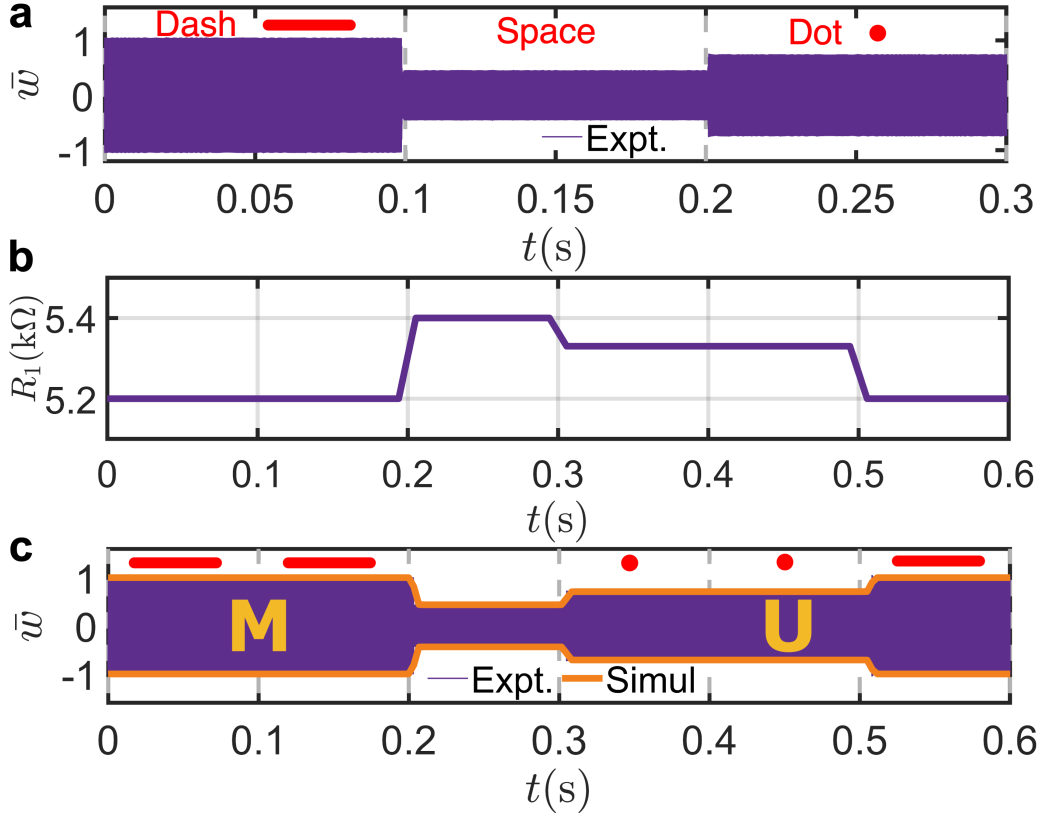


**Figure 7. Time-varying metabeam for morse coding.** **a** Fundamental elements of Morse coding—dash, space, and dot—are created using flexural waves of varying amplitudes. **b** The transfer function corresponds to the Morse code representation of the text "MU". **c** The measured signal (purple lines) is encapsulated by the simulated signal (orange lines), encoding the text "MU".

224 **5a** presents optimal parameters to achieve this task for a temporal multilayer with three slabs, where  $n = [3, 1, 3]n_0$  represents  
 225 the refractive indices and  $t = [0, 0.75, 0.25, 0.75]/f_0$  represents the corresponding time intervals. The initial refractive index  
 226 is denoted by  $n_0$ . These parameters are obtained by minimizing the negative square of the magnitude of the refraction coefficient  
 227 at 6 kHz (see [Supplementary Section 12](#) for details). The length of each slab is a quarter of the wave period, resulting in a phase  
 228 decrease of  $\pi/4$  for the refracted wave and a phase increase of  $\pi/4$  for the reflected wave. After passing through each slab, the  
 229 phase difference between the refracted and reflected waves reaches  $\pi$ , leading to constructive interference at the subsequent  
 230 temporal interface, which amplifies the waves<sup>29</sup>. The wave packet evolution in this medium is shown in Fig. 5b, where  
 231 significant amplification of both refraction and reflection is observed. Fig. 5c shows that the simulated reflection coefficient  
 232 peaks at approximately 4.5 around the frequency  $f_0$ , closely matching the analytical results from the transfer matrix method.  
 233 Although the refraction coefficient is optimized for a specific frequency, amplification is observed over a broad frequency range,  
 234 spanning from  $0.6f_0$  to  $1.4f_0$ .

### 235 Temporal metabeams for smart waveform morphing and information coding

236 In this section, we propose a method for designing temporal metabeams with tunable time-varying bending stiffness by utilizing  
 237 self-reconfigurable transfer functions controlled by time-varying digital potentiometers. By programming the time-domain  
 238 behavior of these digital potentiometers, the metabeam's bending stiffness can be modulated to follow desired periodic or  
 239 aperiodic patterns. The proposed time-varying metabeam demonstrates capabilities in shaping the amplitudes of transmitted  
 240 flexural waves in the time domain, both experimentally and numerically, as illustrated in Fig. 6a. It is essential to emphasize  
 241 that the time-varying parameters must meet adiabatic conditions, meaning the bending stiffness should change gradually enough  
 242 to avoid inducing frequency conversion at the temporal stepped interface.

243 Under the assumption of the length of the unit cell being much shorter than the wavelength, the effective bending stiffness  
 244 of the metabeams could be positive and negative. Previous studies employed metabeams with time-varying negative bending  
 245 stiffness to modulate the amplitude of flexural waves within the subwavelength Bragg bandgap<sup>56,60</sup>. For the metabeam with the  
 246 negative stiffness, the flexural wave will exponentially decay in factor proportional to the magnitude of the effective bending

247 stiffness (see [Supplementary Section 1](#)). Therefore, the negative stiffness of the metabeam with temporal variability spanning a  
248 reasonable range could result in a significant change in wave transmission. The time-varying bending stiffnesses are difficult to  
249 measure directly, hence we indirectly verify the existence by studying the wave transmission properties of the metabeam. To  
250 understand the underlying mechanism of this method, we analyze the influences of the constitutive parameters on the wave  
251 transmission of a metabeam with 30 unit cells.

252 A time-varying transfer function is applied to the metabeam to achieve the desired waveform morphing. For instance,  
253 the transfer function can be modulated as a sinusoidal or smooth step function using a time-varying digital potentiometer, as  
254 shown in Fig. 6b and 6e. For an excitation frequency of 33 kHz, the corresponding effective bending stiffness over time is  
255 plotted in Fig. 6c and 6f. The detailed smooth functions can be found in [Supplementary Section 13](#). The results in Fig. 6c  
256 and 6f show that the modulation pattern of the bending stiffness can be flexibly tuned to any desired shape by programming  
257 the transfer functions. Next, we demonstrate that modulating the constitutive parameters can be used for waveform morphing.  
258 Using sinusoidal and smooth step function patterns as examples, we measure the transmitted waves for different modulation  
259 amplitudes, as shown in Fig. 6d and 6g. As shown in Fig. 6d and 6g, the variations in bending stiffness are clearly reflected in  
260 the changing amplitudes of the transmitted wave, demonstrating that the metabeam can modulate the amplitude of transmitted  
261 signals in a desired periodic manner. The experimental and simulated transmitted wave amplitudes are in excellent agreement,  
262 following the patterns predicted by the homogenized model. This confirms that the adiabatic assumption is satisfied, allowing  
263 the metabeam to be treated as a temporal Cauchy-elastic medium with strongly time-modulated constitutive parameters.

264 As an additional example, we utilize the metabeam as an elastic Morse coder to demonstrate its capability to modulate wave  
265 amplitudes in an aperiodic manner. Morse codes represent letters of the alphabet, numerals, and punctuation marks by arranging  
266 dots, dashes, and spaces, as depicted in Fig. 7a. Traditionally, the codes are transmitted as electric pulse, mechanical or visual  
267 signals. Here, we program the codes with time-varying bending stiffness of the metabeam. These codes are distinguished by  
268 the amplitudes of the transmitted waves when the metabeam is excited on the left side by a constant sine signal at 33 kHz.  
269 Specifically, a "dash" is represented by the measured transmitted wave with the largest amplitude among the three states and it  
270 is normalized to unit 1, as shown in Fig. 7a; a dot is represented by the normalized amplitude of the transmitted wave being  
271 0.75; a space between letters is represented by the amplitude of the transmitted wave being 0.45. In addition, each state is  
272 designed to last 0.1 seconds in the time domain.

273 Using the coding rules, we encode "MU", the abbreviation for the University of Missouri, into the metabeam via a  
274 time-varying transfer function. The time-varying digital potentiometer corresponding to this transfer function is shown in Fig.  
275 7b. The encoded information can be extracted by mechanically stimulating the left side of the metabeam with a constant 33  
276 kHz sine signal and measuring the transmitted wave on the right side. The measured signal, shown in Fig. 7c, successfully  
277 transmits the letters "MU". The measured signals are in excellent agreement with our numerical simulations.

## 278 Discussion

279 This study presents the experimental observation of temporal refraction and reflection of flexural waves in a time-varying  
280 metabeam with time-modulated bending stiffness. We also demonstrated stepped and smooth variations of multiple time  
281 interfaces for enhanced wave control based on time scattering. Our metabeam, composed of an elastic beam with attached  
282 piezoelectric patches, is a mechanical platform well verse to explore a wide range of time-varying media in ultrafast wave  
283 control and advanced signal processing technologies through time-varying transfer functions. The temporal variation patterns  
284 can be of periodic or non-periodic form, allowing for fast and flexible adjustment, and can even be controlled wirelessly.  
285 We have established analogues to Snell's law and Fresnel equations for elastic waves, providing a theoretical framework for  
286 understanding wave scattering at temporal boundaries, which was validated through experimental testing. Due to spatial  
287 translational symmetry, we show that momentum remains conserved, revealing the fundamental principles governing wave  
288 scattering in time-varying media. The rapid modulation of stiffness via elastic elements is scalable and it can be applied to more  
289 complex designs, including damping compensation. A smooth time-varying metabeam was then implemented in waveguides,  
290 achieving anti-reflection temporal coatings, wave morphing, impedance matching, and efficient frequency conversion. Beyond  
291 these remarkable functionalities, the metabeam may serve as a platform to study phenomena like temporal pumping and  $k$ -space  
292 bandgaps, inspiring the development of novel wave-based devices for signal processing.

293 Moving forward, this work opens exciting opportunities, in particular in the context of combining spatial and temporal  
294 interfaces for 4D elastic metamaterials<sup>1</sup>. Opportunities to realize elastic time crystals and quasi-crystals emerge in this platform,  
295 enabling the time analogues of sophisticated spatial wave features such as Hofstadter's butterfly and topological modes.  
296 Time-varying elastodynamic media undoubtedly open new and exciting research avenues for wave control and manipulation,  
297 offering novel degrees of freedom for steering and controlling phases of matter. The elastic wave platform introduced here  
298 offers interesting opportunities to explore these phenomena experimentally.

## 299 Methods

300 **Sample fabrication.** The metabeam is composed of 30 piezoelectric patches (APC 850: 10 mm × 10 mm × 0.8 mm) mounted  
 301 via conductive epoxy onto the middle of an aluminum host beam (180 mm × 10 mm × 2 mm). In the circuit, the resistors  
 302  $R_0 = 1 \text{ M}\Omega$  and  $R_2 = 10 \text{ k}\Omega$  with 5% error, the capacitors are film capacitors with 5% error, the microcontroller is an STM32  
 303 Nucleo Development Board with an STM32F446RE MCU, the digital potentiometer  $R_1$  is a 20 k $\Omega$  AD5291 from Analog  
 304 Devices, and the analog switch is a DG411 from Vishay Siliconix.

305 **Experimental procedures.** In experiments, 30 piezoelectric patches are connected with control circuits, and another piezo-  
 306 electric patch on their left is used to generate incident flexural waves. We employ 3 cycles of tone-burst signals with central  
 307 frequencies at 6 kHz, 8 kHz, and 10 kHz for temporal refraction and reflection. We generate and amplify incident wave signals  
 308 via an arbitrary waveform generator (Tektronix AFG3022C) and a high-voltage amplifier (Krohn-Hite), respectively. Transverse  
 309 velocity wavefields are measured on the surface of the metamaterial by a scanning laser Doppler vibrometer (Polytec PSV-400).  
 310 The analog switch is controlled by the microcontroller to turn off 0.3 ms after the reference signal, generated by the arbitrary  
 311 waveform generator with an amplitude of 3 V, drops below  $-2 \text{ V}$ . For smart waveform morphing, the excitation is applied  
 312 using a sinusoidal signal with a frequency of 33 kHz, and the velocity signal is measured at a position 0.2 m to the right of the  
 313 rightmost piezoelectric patches.

314 **Finite element simulations.** The numerical simulations are conducted by using a 2D "Piezoelectricity, Solid" module in the  
 315 commercial finite element software COMSOL Multiphysics. The material of the host beam is implemented by Aluminum  
 316 [solid] and of piezoelectric patches are PZT-5A from COMSOL Material Library. The current passing through the top surface  
 317 of the piezoelectric patch is coupled with voltage on the top surface by a transfer function using "Global ODEs and DAEs"  
 318 module for simulating the circuit effect. The dispersion curves in Fig. 2h are obtained by using eigenfrequency analysis with  
 319 Floquet boundary conditions. The time domain analysis is conducted for the same setup as the experiment, where the transfer  
 320 function is defined as a time-varying function. The boundary conditions on both sides for temporal refraction and reflection  
 321 are free boundaries. However, two gradient damping beams are attached on both sides to create perfect absorption boundary  
 322 conditions for smart waveform morphing.

323 **Temporal quarter-wave transformer** The temporal quarter-wave transformer comprises a slab with refractive index  $n_1$   
 324 surrounded by two semi-infinite media with refractive indices  $n_0$  and  $n_2$ , respectively. Therefore, the transfer matrix consists of  
 325 two matching matrices and one propagation matrix combined as

$$\mathbf{N} = \begin{bmatrix} T_2 & R_2 \\ R_2 & T_2 \end{bmatrix} \begin{bmatrix} e^{-i\omega_1 \Delta t_1} & 0 \\ 0 & e^{i\omega_1 \Delta t_1} \end{bmatrix} \begin{bmatrix} T_1 & R_1 \\ R_1 & T_1 \end{bmatrix}. \quad (20)$$

326 Eq. (20) gives the reflection coefficient:

$$R = N_{21} = R_1 T_2 e^{i\omega_1 \Delta t_1} + R_2 T_1 e^{-i\omega_1 \Delta t_1}. \quad (21)$$

327 The reflection coefficient can be canceled out through coherent subtraction, which implies

$$R_1 T_2 e^{i\omega_1 \Delta t_1} + R_2 T_1 e^{-i\omega_1 \Delta t_1} = 0. \quad (22)$$

328 This complex equation can be decomposed into two real equations corresponding to the amplitude and the phase:

$$\begin{aligned} \omega_1 \Delta t_1 &= \frac{(2n+1)\pi}{2}, \\ R_2 T_1 &= T_2 R_1. \end{aligned} \quad (23)$$

329 These two equations give the anti-reflection conditions:

$$\begin{aligned} \Delta t_1 &= \frac{(2p+1)}{4f_1}, \\ n_1 &= \sqrt{n_0 n_2}, \end{aligned} \quad (24)$$

330 where  $p$  is an integer, and  $f_1$  is the wave frequency in the middle slab with refractive index  $n_1$ . If  $p = 0$ , the slab length  $\Delta t_1$   
 331 equals a quarter of the wave period, making this temporal medium a quarter-wave transformer. In the main text, with  $n_2 = 2n_0$ ,  
 332 we have  $n_1 = \sqrt{2}n_0$ ,  $f_1 = \sqrt{2}f_0/2$ , and  $t_2 = 1/(2\sqrt{2}f_0)$  for  $p = 0$  and  $t_1 = 0$ .

## 333 References

334 1. Engheta, N. Four-dimensional optics using time-varying metamaterials. *Science* **379**, 1190–1191 (2023).

- 335 **2.** Galiffi, E. *et al.* Photonics of time-varying media. *Adv. Photonics* **4**, 014002–014002 (2022).
- 336 **3.** Yin, S., Galiffi, E. & Alù, A. Floquet metamaterials. *ELight* **2**, 1–13 (2022).
- 337 **4.** Zee, A. *Quantum field theory in a nutshell*, vol. 7 (Princeton university press, 2010).
- 338 **5.** Ortega-Gomez, A., Lobet, M., Vázquez-Lozano, J. E. & Liberal, I. Tutorial on the conservation of momentum in photonic  
339 time-varying media. *Opt. Mater. Express* **13**, 1598–1608 (2023).
- 340 **6.** Miyamaru, F. *et al.* Ultrafast frequency-shift dynamics at temporal boundary induced by structural-dispersion switching of  
341 waveguides. *Phys. Rev. Lett.* **127**, 053902 (2021).
- 342 **7.** Lyubarov, M. *et al.* Amplified emission and lasing in photonic time crystals. *Science* **377**, 425–428 (2022).
- 343 **8.** Dikopoltsev, A. *et al.* Light emission by free electrons in photonic time-crystals. *Proc. Natl. Acad. Sci.* **119**, e2119705119  
344 (2022).
- 345 **9.** Vázquez-Lozano, J. E. & Liberal, I. Incandescent temporal metamaterials. *Nat. Commun.* **14**, 4606 (2023).
- 346 **10.** Horsley, S. A. & Pendry, J. B. Quantum electrodynamics of time-varying gratings. *Proc. Natl. Acad. Sci.* **120**, e2302652120  
347 (2023).
- 348 **11.** Koutserimpas, T. T. & Monticone, F. Time-varying media, dispersion, and the principle of causality. *Opt. Mater. Express*  
349 **14**, 1222–1236 (2024).
- 350 **12.** Li, H., Mekawy, A. & Alù, A. Beyond chu’s limit with floquet impedance matching. *Phys. Rev. Lett.* **123**, 164102 (2019).
- 351 **13.** Hayran, Z. & Monticone, F. Beyond the rozanov bound on electromagnetic absorption via periodic temporal modulations.  
352 *Phys. Rev. Appl.* **21**, 044007 (2024).
- 353 **14.** Yang, X., Wen, E. & Sievenpiper, D. F. Broadband time-modulated absorber beyond the bode-fano limit for short pulses by  
354 energy trapping. *Phys. Rev. Appl.* **17**, 044003 (2022).
- 355 **15.** Akhmanov, S., Sukhorukov, A. & Chirkin, A. Nonstationary phenomena and space-time analogy in nonlinear optics. *Sov.*  
356 *Phys. JETP* **28**, 748–757 (1969).
- 357 **16.** Kolner, B. H. Space-time duality and the theory of temporal imaging. *IEEE J. Quantum Electron.* **30**, 1951–1963 (1994).
- 358 **17.** Lustig, E. *et al.* Photonic time-crystals-fundamental concepts. *Opt. Express* **31**, 9165–9170 (2023).
- 359 **18.** Morgenthaler, F. R. Velocity modulation of electromagnetic waves. *IRE Transactions on microwave theory techniques* **6**,  
360 167–172 (1958).
- 361 **19.** Moussa, H. *et al.* Observation of temporal reflection and broadband frequency translation at photonic time interfaces. *Nat.*  
362 *Phys.* 1–6 (2023).
- 363 **20.** Dong, Z. *et al.* Quantum time reflection and refraction of ultracold atoms. *Nat. Photonics* **18**, 68–73 (2024).
- 364 **21.** Jones, T. R., Kildishev, A. V., Segev, M. & Peroulis, D. Time-reflection of microwaves by a fast optically-controlled  
365 time-boundary. *Nat. Commun.* **15**, 6786 (2024).
- 366 **22.** Qin, C. *et al.* Observation of discrete-light temporal refraction by moving potentials with broken galilean invariance. *Nat.*  
367 *Commun.* **15**, 5444 (2024).
- 368 **23.** Pacheco-Peña, V. & Engheta, N. Antireflection temporal coatings. *Optica* **7**, 323–331 (2020).
- 369 **24.** Pacheco-Peña, V. & Engheta, N. Temporal equivalent of the brewster angle. *Phys. Rev. B* **104**, 214308 (2021).
- 370 **25.** Ponomarenko, S. A., Zhang, J. & Agrawal, G. P. Goos-hänchen shift at a temporal boundary. *Phys. Rev. A* **106**, L061501  
371 (2022).
- 372 **26.** Qin, C. *et al.* Temporal goos-hänchen shift in synthetic discrete-time heterolattices. *Phys. Rev. Lett.* **133**, 083802 (2024).
- 373 **27.** Bacot, V., Labousse, M., Eddi, A., Fink, M. & Fort, E. Time reversal and holography with spacetime transformations. *Nat.*  
374 *Phys.* **12**, 972–977 (2016).
- 375 **28.** Tirole, R. *et al.* Double-slit time diffraction at optical frequencies. *Nat. Phys.* 1–4 (2023).
- 376 **29.** Galiffi, E. *et al.* Broadband coherent wave control through photonic collisions at time interfaces. *Nat. Phys.* **19**, 1703–1708  
377 (2023).
- 378 **30.** Wilczek, F. Quantum time crystals. *Phys. Rev. Lett.* **109**, 160401 (2012).
- 379 **31.** Zaletel, M. P. *et al.* Colloquium: Quantum and classical discrete time crystals. *Rev. Mod. Phys.* **95**, 031001 (2023).
- 380 **32.** Kongkhambut, P. *et al.* Observation of a continuous time crystal. *Science* **377**, 670–673 (2022).

- 381 **33.** Carminati, R., Chen, H., Pierrat, R. & Shapiro, B. Universal statistics of waves in a random time-varying medium. *Phys.*  
382 *Rev. Lett.* **127**, 094101 (2021).
- 383 **34.** Sharabi, Y., Lustig, E. & Segev, M. Disordered photonic time crystals. *Phys. Rev. Lett.* **126**, 163902 (2021).
- 384 **35.** Apffel, B., Wildeman, S., Eddi, A. & Fort, E. Experimental implementation of wave propagation in disordered time-varying  
385 media. *Phys. Rev. Lett.* **128**, 094503 (2022).
- 386 **36.** Trainiti, G. *et al.* Time-periodic stiffness modulation in elastic metamaterials for selective wave filtering: Theory and  
387 experiment. *Phys. Rev. Lett.* **122**, 124301 (2019).
- 388 **37.** Lustig, E., Sharabi, Y. & Segev, M. Topological aspects of photonic time crystals. *Optica* **5**, 1390–1395 (2018).
- 389 **38.** Pan, Y., Cohen, M.-I. & Segev, M. Superluminal k-gap solitons in nonlinear photonic time crystals. *Phys. Rev. Lett.* **130**,  
390 233801 (2023).
- 391 **39.** Chong, C., Kim, B., Wallace, E. & Daraio, C. Modulation instability and wavenumber bandgap breathers in a time layered  
392 phononic lattice. *Phys. Rev. Res.* **6**, 023045 (2024).
- 393 **40.** Galiffi, E., Yin, S. & Alú, A. Tapered photonic switching. *Nanophotonics* **11**, 3575–3581 (2022).
- 394 **41.** Pang, K. *et al.* Adiabatic frequency conversion using a time-varying epsilon-near-zero metasurface. *Nano Lett.* **21**,  
395 5907–5913 (2021).
- 396 **42.** Khurgin, J. B. *et al.* Adiabatic frequency shifting in epsilon-near-zero materials: the role of group velocity. *Optica* **7**,  
397 226–231 (2020).
- 398 **43.** Chen, H., Yao, L., Nassar, H. & Huang, G. Mechanical quantum hall effect in time-modulated elastic materials. *Phys. Rev.*  
399 *Appl.* **11**, 044029 (2019).
- 400 **44.** Wang, S. *et al.* Smart patterning for topological pumping of elastic surface waves. *Sci. Adv.* **9**, eadh4310 (2023).
- 401 **45.** Chen, Z.-G., Zhang, R.-Y., Chan, C. T. & Ma, G. Classical non-abelian braiding of acoustic modes. *Nat. Phys.* **18**, 179–184  
402 (2022).
- 403 **46.** Yang, Y. *et al.* Non-abelian physics in light and sound. *Science* **383**, eadf9621 (2024).
- 404 **47.** Delory, A. *et al.* Elastic wavepackets crossing a space-time interface. *arXiv preprint arXiv:2406.15100* (2024).
- 405 **48.** Kim, B. L., Chong, C. & Daraio, C. Temporal refraction in an acoustic phononic lattice. *Phys. Rev. Lett.* **133**, 077201  
406 (2024).
- 407 **49.** Chen, Y., Li, X., Scheibner, C., Vitelli, V. & Huang, G. Realization of active metamaterials with odd micropolar elasticity.  
408 *Nat. Commun.* **12**, 5935 (2021).
- 409 **50.** Wu, Q. *et al.* Active metamaterials for realizing odd mass density. *Proc. Natl. Acad. Sci.* **120**, e2209829120 (2023).
- 410 **51.** Chen, Y., Li, X., Hu, G., Haberman, M. R. & Huang, G. An active mechanical willis meta-layer with asymmetric  
411 polarizabilities. *Nat. Commun.* **11**, 3681 (2020).
- 412 **52.** Wu, Q., Zhang, X., Shivashankar, P., Chen, Y. & Huang, G. Independent flexural wave frequency conversion by a linear  
413 active metalayer. *Phys. Rev. Lett.* **128**, 244301 (2022).
- 414 **53.** Xia, Y. *et al.* Experimental observation of temporal pumping in electromechanical waveguides. *Phys. Rev. Lett.* **126**,  
415 095501 (2021).
- 416 **54.** Hagood, N. W. & Von Flotow, A. Damping of structural vibrations with piezoelectric materials and passive electrical  
417 networks. *J. Sound Vib.* **146**, 243–268 (1991).
- 418 **55.** Marconi, J. *et al.* Experimental observation of nonreciprocal band gaps in a space-time-modulated beam using a shunted  
419 piezoelectric array. *Phys. Rev. Appl.* **13**, 031001 (2020).
- 420 **56.** Chen, Y., Hu, G. & Huang, G. A hybrid elastic metamaterial with negative mass density and tunable bending stiffness. *J.*  
421 *Mech. Phys. Solids* **105**, 179–198 (2017).
- 422 **57.** Castaldi, G., Pacheco-Peña, V., Moccia, M., Engheta, N. & Galdi, V. Exploiting space-time duality in the synthesis of  
423 impedance transformers via temporal metamaterials. *Nanophotonics* **10**, 3687–3699 (2021).
- 424 **58.** Ramaccia, D., Alù, A., Toscano, A. & Bilotti, F. Temporal multilayer structures for designing higher-order transfer  
425 functions using time-varying metamaterials. *Appl. Phys. Lett.* **118** (2021).
- 426 **59.** Collin, R. E. *Foundations for microwave engineering* (John Wiley & Sons, 2007).
- 427 **60.** Chen, Y., Zhu, R., Barnhart, M. V. & Huang, G. Enhanced flexural wave sensing by adaptive gradient-index metamaterials.  
428 *Sci. Reports* **6**, 35048 (2016).

## 429 **Data availability**

430 All data that support the plots within this paper and other findings of this study are available from the corresponding author  
431 upon reasonable request. Source data are provided with this paper.

## 432 **Code availability**

433 The codes that support the findings of this study are available from the corresponding author upon reasonable request.

## 434 **Acknowledgements**

435 G.H. acknowledges the support by the Air Force Office of Scientific Research under Grant No. AF 9550-18-1-0342 and AF  
436 9550-20-1-0279 with Program Manager Dr. Gregg Abate. A.A. is supported by the NSF Science and Technology Center  
437 'Frontiers of Sound' and the Simons Foundation.

## 438 **Author contributions statement**

439 S.W., N.S., and H.Q. designed the metabeam with integrated circuits and conducted the simulations and measurements. S.W.  
440 and H.C. developed the theoretical framework, with contributions from Q.W., A.A., and G.H. S.W., J.C., A.A., H.D. and G.H.  
441 interpreted and presented the experimental data. S.W. and G.H. led the writing of the paper and the Supplementary Information,  
442 with input from all authors. The problem was conceived by S.W., A.A., and G.H., and the project was supervised by G.H.



# Time transmission and time reflection in temporal mechanical metabeams: theory and their application

Shaoyun Wang,<sup>1,\*</sup> Nan Shao,<sup>1,\*</sup> Hui Chen,<sup>2</sup> Jiaji Chen,<sup>1</sup> Honghua Qian,<sup>1</sup>  
Qian Wu,<sup>1</sup> Huilin Duan,<sup>3</sup> Andrea Alù,<sup>4,5,†</sup> and Guoliang Huang<sup>3,‡</sup>

<sup>1</sup>*Department of Mechanical and Aerospace Engineering,  
University of Missouri, Columbia, MO 65211, USA*

<sup>2</sup>*Center for Mechanics Plus under Extreme Environments,  
School of Mechanical Engineering and Mechanics, Ningbo University, Ningbo 315211, China*

<sup>3</sup>*Department of Mechanics and Engineering Science,  
College of Engineering, Peking University, Beijing 100871, PR China*

<sup>4</sup>*Photonics Initiative, Advanced Science Research Center,  
City University of New York, New York, NY, USA*

<sup>5</sup>*Physics Program, Graduate Center, City University of New York, New York, NY, USA*  
(Dated: December 15, 2024)

## CONTENTS

|  |    |
|--|----|
| 1. Determine the effective bending stiffness from numerical tests  | 2  |
| 2. Experimental details  | 2  |
| A. Geometric and material parameters of the metabeam   | 2  |
| B. Experiment layout and measurement setup   | 4  |
| 3. Verification of temporal reflection in the experiment   | 5  |
| 4. Numerical simulation of temporal refraction and reflection  | 6  |
| A. Numerical simulation of temporal refraction and reflection in a metabeam                              | 6  |
| B. Numerical simulation of temporal refraction and reflection in a long metabeam                         | 7  |
| 5. Refraction and reflection at a time interface for the switch from OFF to ON in experiment             | 8  |
| 6. Refraction and reflection at a time interface for different frequencies in the experiment             | 9  |
| 7. Numerical investigation of the effect of finite switching time  | 11 |
| 8. Numerical study of temporal refraction and reflection of an asymmetric pulse                          | 11 |
| 9. Derivation of temporal continuity conditions  | 11 |
| 10. Relationship between the angles of incidence and refraction  | 13 |
| 11. Noether's theorem and conservation laws  | 14 |
| A. Complex scalar field theory for the Euler-Bernoulli beam  | 14 |
| B. Time translation symmetry and energy conservation   | 16 |
| C. Space translation symmetry and momentum conservation  | 17 |
| 12. Optimization method for broadband anti-reflection and wave amplification at multiple time interfaces | 18 |
| 13. Resistor functions in smart waveform morphing and information  | 19 |
| References   | 19 |

\* These two authors contributed equally.

† Corresponding author: [aalu@cuny.edu](mailto:aalu@cuny.edu)

‡ Corresponding author:

[guohuang@pku.edu.cn](mailto:guohuang@pku.edu.cn), [glhuang911@gmail.com](mailto:glhuang911@gmail.com)

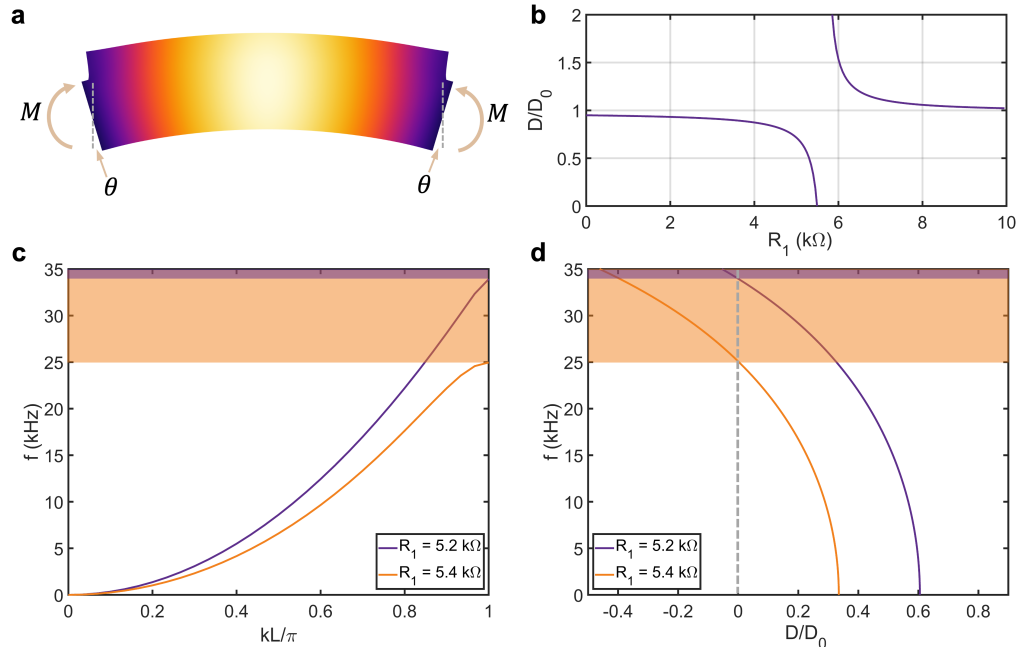


FIG. S1. **The effective bending stiffness and its application.** **a** Setup for determining the effective stiffness in the numerical test. **b** The relationship between normalized effective stiffness and  $R_1$ .  $D_0$  represents the bending stiffness for the open circuit. **c** The dispersion curves for different values of  $R_1$ . The purple region indicates the bandgap for  $R_1 = 5.2 \text{ k}\Omega$ , while the orange region indicates the bandgap for  $R_1 = 5.4 \text{ k}\Omega$ . **d** The normalized stiffness as a function of frequency. The purple region shows the negative stiffness area for  $R_1 = 5.2 \text{ k}\Omega$ , and the orange region shows the negative stiffness area for  $R_1 = 5.4 \text{ k}\Omega$ .

## 1. DETERMINE THE EFFECTIVE BENDING STIFFNESS FROM NUMERICAL TESTS

A schematic diagram of the numerical test is shown in Fig. S1a. To determine the effective bending stiffness, the rotational angles at the left and right boundaries of the metabeam unit cell are set to  $-\theta$  and  $\theta$ , respectively, using rigid connectors in COMSOL. The vertical displacements at both boundaries are constrained to zero, while the horizontal displacements are left free. The reaction bending moment  $M$  at each rigid connector is obtained for calculating the effective bending stiffness. By solving the problem in the frequency domain, the effective bending stiffness  $D$  of the metabeam is defined following the approach described by Chen [1]:

$$D = \frac{M}{2\theta/L}, \quad (\text{S1})$$

where  $L$  is the length of the unit cell. The normalized effective bending stiffness as a function of the resistor  $R_1$  is shown in Fig. S1b. For  $R_1$  values smaller than  $5.5 \text{ k}\Omega$ , the normalized stiffness decreases to zero as  $R_1$  increases, demonstrating the potential for tuning the bending stiffness using the negative capacitance circuit. For temporal refraction and reflection,  $R_1 = 5 \text{ k}\Omega$ , resulting in a normalized stiffness of  $D/D_0 = 0.72$  at the operating frequency of  $6 \text{ kHz}$ , where  $D_0 = 0.88 \text{ N} \cdot \text{m}^2$ . In general, the bending stiffness is frequency-dependent, and negative bending stiffness indicates the presence of bandgaps. As shown in Fig. S1c,d, the range of bandgaps corresponds to the range of negative normalized effective stiffness for different  $R_1$  values. Additionally, the average density of the metabeam is  $4143 \text{ kg/m}^3$ , and  $\rho A = 0.116 \text{ kg/m}$ .

## 2. EXPERIMENTAL DETAILS

### A. Geometric and material parameters of the metabeam

The metabeam consists of 30 unit cells, each equipped with a piezoelectric patch connected to a negative capacitance circuit via an analog switch, along with an additional unit cell used for excitation, as illustrated in Fig. S2a. The 30

TABLE S1. Geometric and material parameters of the metabeam.

| Parameter         | Description                                    | Value                        |
|-------------------|--|------------------------------|
| $h_b$             | Thickness of the host beam                     | 2 mm                         |
| $w_b$             | Width of the host beam                         | 1 cm                         |
| $L_p$             | Length of the piezoelectric patches            | 1 cm                         |
| $h_p$             | Thickness of the piezoelectric patches         | 0.8 mm                       |
| $w_p$             | Width of the piezoelectric patches             | 1 cm                         |
| $\Delta L$        | Interval between two piezoelectric patches     | 0.67 mm                      |
| $E_b$             | Young's modulus of the aluminum beam           | 70 GPa                       |
| $\rho_b$          | Density of the aluminum beam                   | 2700 kg/m <sup>3</sup>       |
| $s_{11}^E$        | Compliance matrix of the piezoelectric patches | $1.64 \times 10^{-11}$ 1/Pa  |
| $s_{33}^E$        | Compliance matrix of the piezoelectric patches | $1.88 \times 10^{-11}$ 1/Pa  |
| $s_{44}^E$        | Compliance matrix of the piezoelectric patches | $4.75 \times 10^{-11}$ 1/Pa  |
| $s_{66}^E$        | Compliance matrix of the piezoelectric patches | $4.43 \times 10^{-11}$ 1/Pa  |
| $s_{12}^E$        | Compliance matrix of the piezoelectric patches | $-5.74 \times 10^{-12}$ 1/Pa |
| $s_{13}^E$        | Compliance matrix of the piezoelectric patches | $-7.22 \times 10^{-12}$ 1/Pa |
| $d_{33}$          | Coupling matrix of the piezoelectric patches   | $3.74 \times 10^{-11}$ C/N   |
| $d_{31}$          | Coupling matrix of the piezoelectric patches   | $-1.71 \times 10^{-11}$ C/N  |
| $d_{15}$          | Coupling matrix of the piezoelectric patches   | $5.84 \times 10^{-11}$ C/N   |
| $\epsilon_{33}^S$ | Coupling matrix of the piezoelectric patches   | 919.1 $\epsilon_0$           |
| $\epsilon_{11}^S$ | Coupling matrix of the piezoelectric patches   | 826.6 $\epsilon_0$           |
| $\epsilon_0$      | Vacuum permittivity                            | $8.842 \times 10^{-12}$ F/m  |
| $\rho_p$          | Density of the piezoelectric patches           | 7750 kg/m <sup>3</sup>       |

TABLE S2. List of components used to fabricate metabeam, referred to the schematic shown in Fig. S2.

| Component             | Description          | Value         |
|-----------------------|----------------------|---------------|
| $C_0$                 | NC circuit capacitor | 1 nF          |
| $R_0$                 | NC circuit resistor  | 1 M $\Omega$  |
| $R_1$                 | NC circuit resistor  | 5 k $\Omega$  |
| $R_2$                 | NC circuit resistor  | 10 k $\Omega$ |
| Analog switch         | DG411                |               |
| Operational amplifier | OPA445               |               |
| MCU                   | STM32F446            |               |

TABLE S3. The angles of the incident wave, refracted wave, and reflected wave.

| Cases               | $\alpha_0$ | $\alpha_1$ | $\alpha'_1$ |
|---------------------|------------|------------|-------------|
| ON-to-OFF at 6 kHz  | 49.0°      | 52.0°      | 52.5°       |
| ON-to-OFF at 6 kHz  | 48.0°      | 43.0°      | 43.5°       |
| ON-to-OFF at 8 kHz  | 40.5°      | 43.5°      | 43.5°       |
| OFF-to-ON at 8 kHz  | 45.0°      | 40.0°      | 40.0°       |
| ON-to-OFF at 10 kHz | 42.0°      | 45.5°      | 45.0°       |
| OFF-to-ON at 10 kHz | 42.0°      | 39.0°      | 39.5°       |

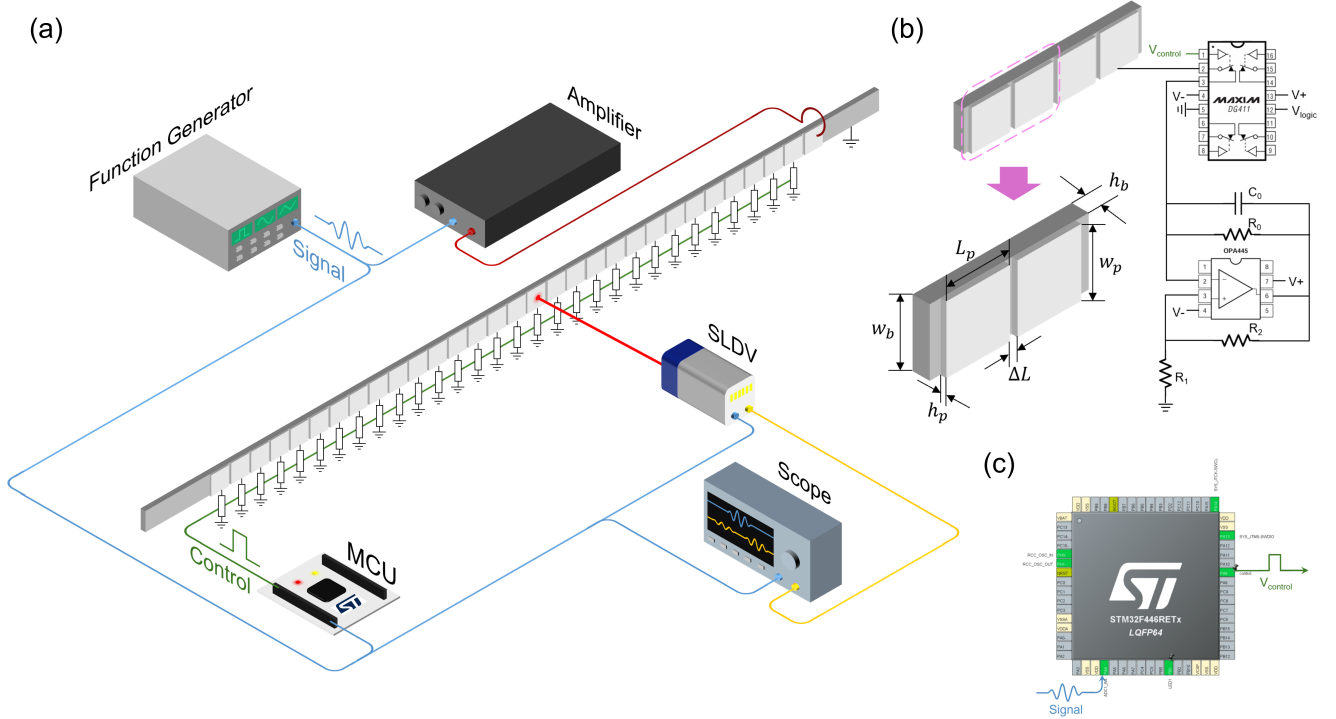


FIG. S2. **Practical experiment layout and measurement setup.** **a** Simplified schematic of the experimental setup. A signal generated by a function generator is amplified by a power amplifier to produce elastic waves through a piezoelectric patch. This signal also triggers an MCU to control all analog switches and activates the scanning laser Doppler vibrometer (SLDV) to measure the transverse velocity of the metabeam’s surface. **b** Electrical control circuit layout and schematic for a single unit cell, along with its geometric parameters. **c** MCU pinout view.

piezoelectric patches are bonded to the aluminum beam using conductive epoxy, which is cured at room temperature for 24 hours. The spacing between adjacent piezoelectric patches is 0.67 mm. The geometric and material parameters of the metabeam, shown in Fig. S2b, are summarized in Table S1.

## B. Experiment layout and measurement setup

An electric signal generated by a function generator (Tektronix AFG3022C) is amplified by a power amplifier (Krohn-Hite) to excite elastic waves via the piezoelectric patch at rightmost. This signal simultaneously triggers a microcontroller unit (STM32F446RE) to control the analog switches and activates the scanning laser Doppler vibrometer (Polytec PSV-400) to measure the transverse velocity on the surface of the metabeam, as illustrated in Fig. S2a. A photograph of the experimental setup, showing the metabeam and its circuits, is presented in Fig. S3.

The laser Doppler vibrometer records data for 25.6 ms at a sampling rate of  $f_s = 1.28$  MHz. The scanned domain, spanning 1.38 m, is discretized into a grid of 219 evenly spaced points, achieving a spatial resolution of 0.0063 m. Fig. S2b provides a schematic of the electrical control system used in each unit cell. The connection status between the piezoelectric patches and the negative capacitance circuits is controlled by analog switches, allowing adjustment of the effective stiffness of the metabeam. When  $V_{\text{control}}$  is at a high voltage level, the switch is OFF, and it is ON at a low voltage level. The switching time is less than 150 ns for transitions from OFF to ON and less than 100 ns for transitions from ON to OFF. These times are approximately 1000 times shorter than the bending wave period (about 150  $\mu$ s), creating an ideal temporal interface.

All electrical circuits are constructed on solderless breadboards. The pinout of the MCU is shown in Fig. S2c. The MCU receives the reference signal through the analog-to-digital converter (ADC) at a sampling rate of 2 MHz. Once the voltage of the reference signal exceeds a specified threshold ( $-2$  V), the MCU changes the state of the analog switch after a precisely programmed delay. The circuit parameters and components are detailed in Table S2.

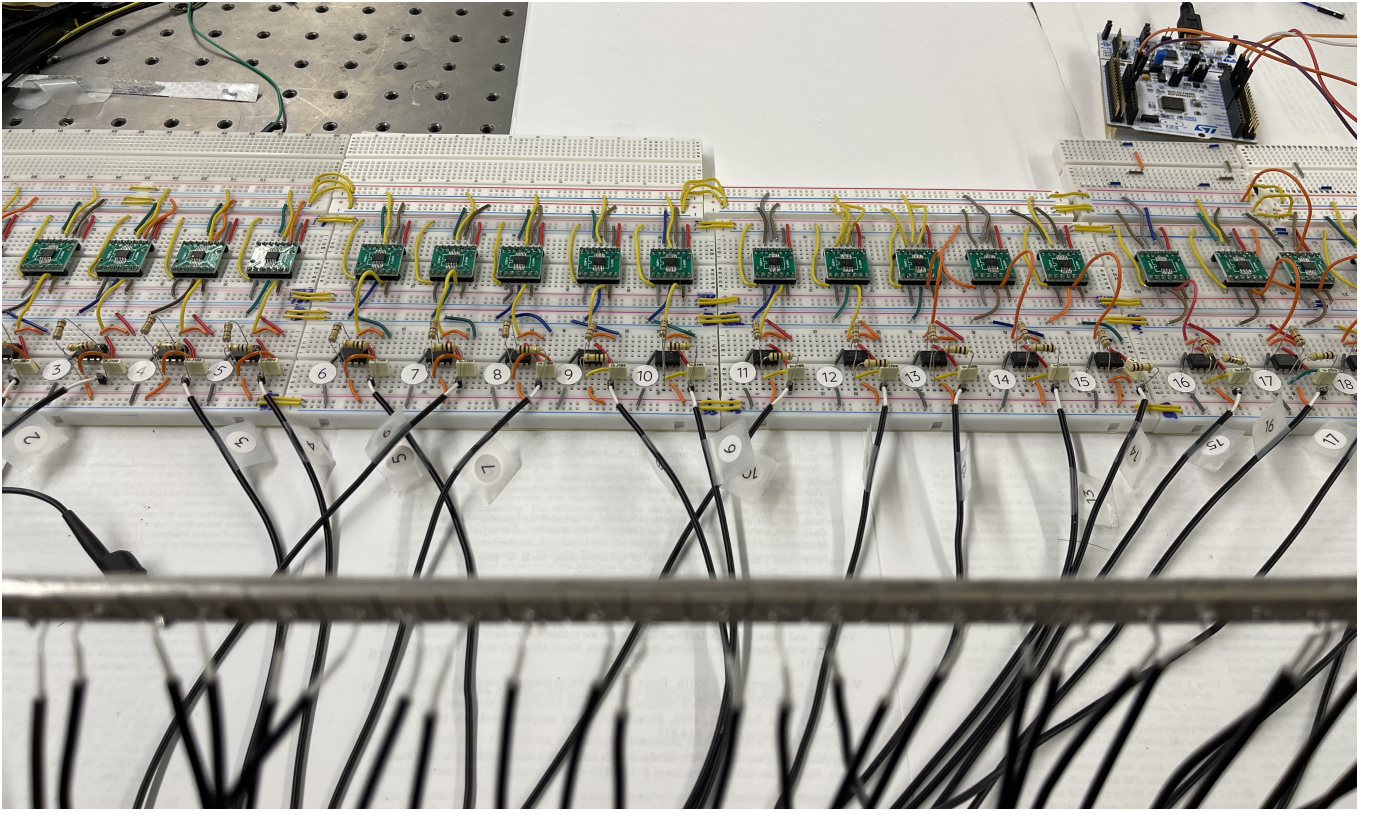


FIG. S3. A photograph of metabeam with circuits.

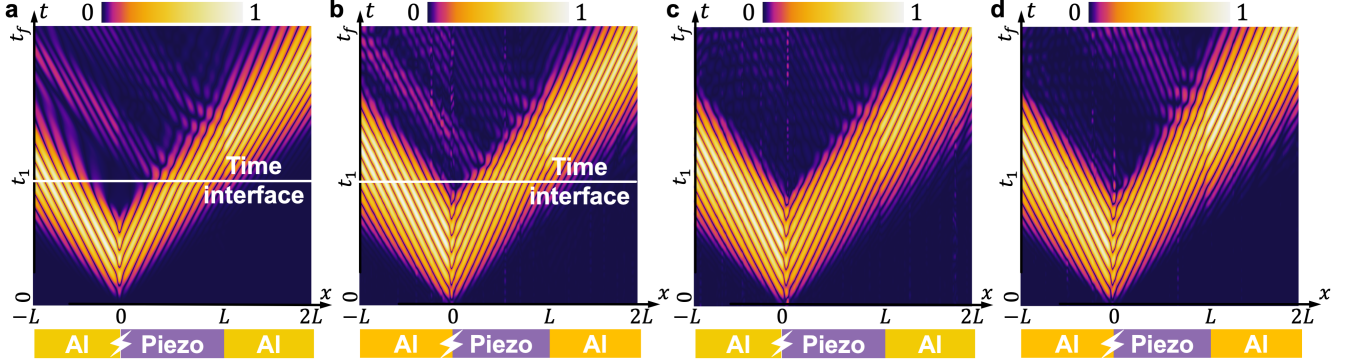


FIG. S4. **Spacetime diagram of temporal refraction and reflection without masks.** **a, b** The top panels show the simulation **(a)** and experimental results **(b)** of wave scattering from an incident wave packet consisting of 3 cycles in the time domain, with parameters  $t_f = 1.1$  ms and  $t_1 = 0.44$  ms, at a time interface in a spacetime diagram. The bottom panels depict the system configuration, consisting of a length  $L = 0.32$  m, composed of two aluminum beams (Al) and a piezo-metabeam (Piezo). The excitation source (indicated by the lightning symbol) is positioned at the left interface. **c, d** The spacetime diagrams illustrate the wave evolution with the switch permanently OFF **(c)** and permanently ON **(d)**.

### 3. VERIFICATION OF TEMPORAL REFLECTION IN THE EXPERIMENT

In Fig. 2a,c of the main text, masks were added to highlight the temporally reflected wave. Here, the masks are removed, and the original figures are presented in Fig. S4a,b. Since the behavior of spatially reflected waves, caused by spatial inhomogeneity, closely resembles that of temporally reflected waves, it is crucial to verify that the reflected waves in Fig. S4a,b are indeed temporally reflected waves rather than spatially reflected waves.

First, we perform a numerical simulation using the same setup as the experiment. The wave evolution in the

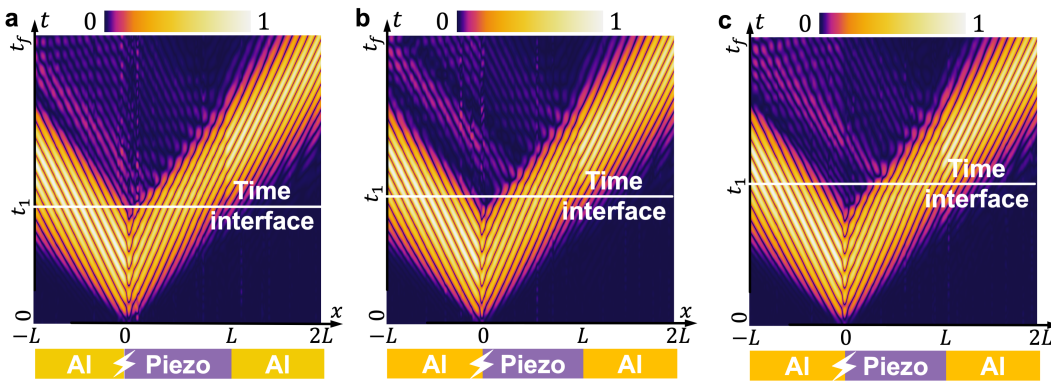


FIG. S5. **Temporal refraction and reflection at different switching times.** **a**, **b**, and **c** show the spacetime diagrams of wave evolution for switching times  $t_1 = 0.435$  ms,  $t_1 = 0.44$  ms, and  $t_1 = 0.445$  ms, respectively.

spacetime diagram from the simulation is shown in Fig. S4a. Since the excitation is applied at the left interface between the aluminum beam and the piezoelectric metabeam, both a left-propagating wave and a right-propagating wave are generated. When the right-propagating wave reaches the right interface between the piezoelectric metabeam and the aluminum beam, a reflected wave is produced due to the spatial interface. In the simulation, an additional reflected wave is generated at the time interface, which is distinct from both the left-propagating wave caused by the excitation and the spatially reflected wave. This temporally reflected wave, also observed in the experiment (see Fig. S4b), closely resembles the one in the simulation, suggesting that it is indeed the time-reflected wave.

In the experiment, the piezoelectric metabeam consists of 30 unit cells, making it challenging to achieve perfect homogeneity across all cells. This inhomogeneity can potentially induce spatially reflected waves within the metabeam. To rule out this possibility, the spacetime diagrams of wave evolution with the switch permanently OFF and ON are presented in Fig. S4c,d for comparison. In these figures, no spatially reflected waves are observed in the middle of the metabeam, indicating that the metabeam is homogeneous. The homogeneity of the metabeam is ensured through the following steps. When the switch is OFF, homogeneity is maintained by carefully attaching the piezoelectric patches at constant intervals. When the switch is ON, resistors with  $R_1 = 5$  k $\Omega$  are initially used, and the spacetime diagram is measured. While the metabeam is generally homogeneous, a few unit cells exhibit stiffness variations, leading to spatially reflected waves visible in the diagram. These abnormal cells are identified, and their resistors are replaced with potentiometers. By tuning the potentiometers until the reflected signals disappear from the PSV-400 screen, uniformity is achieved.

Furthermore, a key characteristic of a temporally reflected wave is that its position depends on the timing of the time interface. To verify this, we conduct three experimental tests with switching times of  $t_1 = 0.435$  ms, 0.44 ms, and 0.445 ms, as shown in Fig. S5. In these figures, the position of the reflected wave shifts with changes in the time interface, confirming that the reflected wave depends on the time interface. This observation indicates that it is a temporally reflected wave rather than a spatially reflected one.

Based on these observations, we conclude that the reflected wave is a temporally reflected wave rather than a spatially reflected wave.

## 4. NUMERICAL SIMULATION OF TEMPORAL REFRACTION AND REFLECTION

### A. Numerical simulation of temporal refraction and reflection in a metabeam

In Fig. 2 of the main text, only the experimental results are presented. Here, the corresponding simulation results are shown in Fig. S6 for comparison. The simulation results in Fig. S6 closely align with the experimental results in Fig. 3 of the main text. The frequency of the refracted and reflected waves is approximately  $1.13 f_0$ , which is close to the theoretical value of  $1.17 f_0$ . Furthermore, the normalized amplitude of the reflected wave with respect to the wave number is flatter and closely matches the theoretical prediction, indicating that the amplitude relation predicted in Eq. (9) of the main text holds over a wide frequency range.

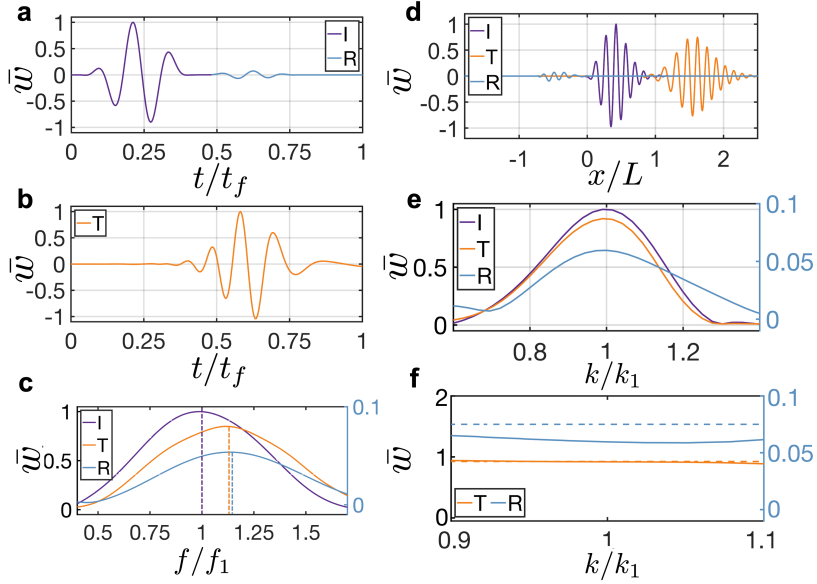


FIG. S6. **Spectral analysis of wave refraction and reflection at a time interface based on numerical simulation data.** **a** The incident (purple) and reflected (blue) signals measured at  $x = 0.05L$ . **b** The refracted signal (orange) observed at  $x = L$ . **c** Spectral analysis of the time-domain signals from (a, b). **d** The incident spatial profile (purple) measured at  $t = 1/3t_f$ , and the reflected and transmitted spatial profiles (blue and orange, respectively) measured at  $t = 2/3t_f$ . **e** Spectral analysis of the spatial-domain signals from (d). **f** The normalized spectral data for the incident, reflected, and refracted waves from (e), with each normalized by the amplitude distribution of the incident wave.

## B. Numerical simulation of temporal refraction and reflection in a long metabeam

In the experiment, the metabeam's normalized stiffness can be reduced to a minimum of 0.72, resulting in a relatively small reflected wave. To better observe temporal refraction and reflection, we perform a simulation using a long metabeam with 240 unit cells, excited by a 5-cycle tone burst. In the simulation, the switch transitions from OFF to ON, with the bending stiffness in the ON state being one-quarter of that in the OFF state. Under these conditions, the refractive index ratio is  $n_1/n_0 = 2$ , and the impedance ratio is  $Z_1/Z_0 = 1/2$ .

In Fig. S7a, the incident wave splits into a refracted wave and a reflected wave upon encountering the time interface. A 2D Fourier transform is applied to the data in Fig. S7a, with the results shown in Fig. S7b. In Fig. S7b, the frequency of the incident wave shifts from  $f_0$  to  $f_0/2$  and  $-f_0/2$ , while the wavenumber remains constant. In Fig. S7c, the directions of the incident, refracted, and reflected plane waves (solid arrows) and wave packets (dashed arrows) are derived from their respective components in Fig. S7a. The incident angle of the plane waves is  $\alpha_i = 42^\circ$ , with refracted and reflected angles of  $\alpha_t = 24^\circ$  and  $\alpha_r = 24^\circ$ , respectively. The ratio  $\tan \alpha_t / \tan \alpha_i = 2.02$  closely matches the refractive index ratio  $n_1/n_0 = 2$ , verifying Snell's law in Eq. (S12) of the main text. For the wave packet, the incident angle is  $\beta_i = 61^\circ$ , while the refracted and reflected angles are  $\beta_t = 43^\circ$  and  $\beta_r = 43^\circ$ , respectively. The ratio  $\tan \beta_t / \tan \beta_i = 1.93$  is close to the refractive index ratio, validating the geometric relationship of the wave packet described in Eq. (S13) of the main text.

Next, we validate the Fresnel equations presented in Eq. (9) of the main text. In Fig. S7d, the incident wave splits into a refracted wave and a reflected wave in the time domain. In the frequency domain, as shown in Fig. S7e, the frequencies of the refracted and reflected waves are approximately half that of the incident wave, quantitatively confirming the frequency shift after passing through the temporal interface, as described in Eq. (7) of the main text. In Fig. S7f, the incident wave splits into a refracted wave and a reflected wave in the spatial domain. The spectral data from Fig. S7f is presented in Fig. S7g. The wavenumbers of the waves remain constant, indicating momentum conservation. The peak amplitude shifts from 1 in the incident wave to 1.5 in the refracted wave and 0.5 in the reflected wave, aligning with the results calculated using the Fresnel equations in Eq. (9) of the main text.

Furthermore, Fig. S7h presents the normalized amplitude distributions of the incident, transmitted, and reflected waves, with each normalized by the amplitude of the incident wave. This confirms that the amplitude ratio is independent of the wavenumber (frequency), as predicted by Eq. (7) of the main text. Additionally, the phase factors are deduced from the wave packet dynamics shown in Fig. S7i. The phase of the transmitted wave remains unchanged relative to the incident wave, while the phase of the reflected wave shifts by  $\pi$  relative to the incident wave across

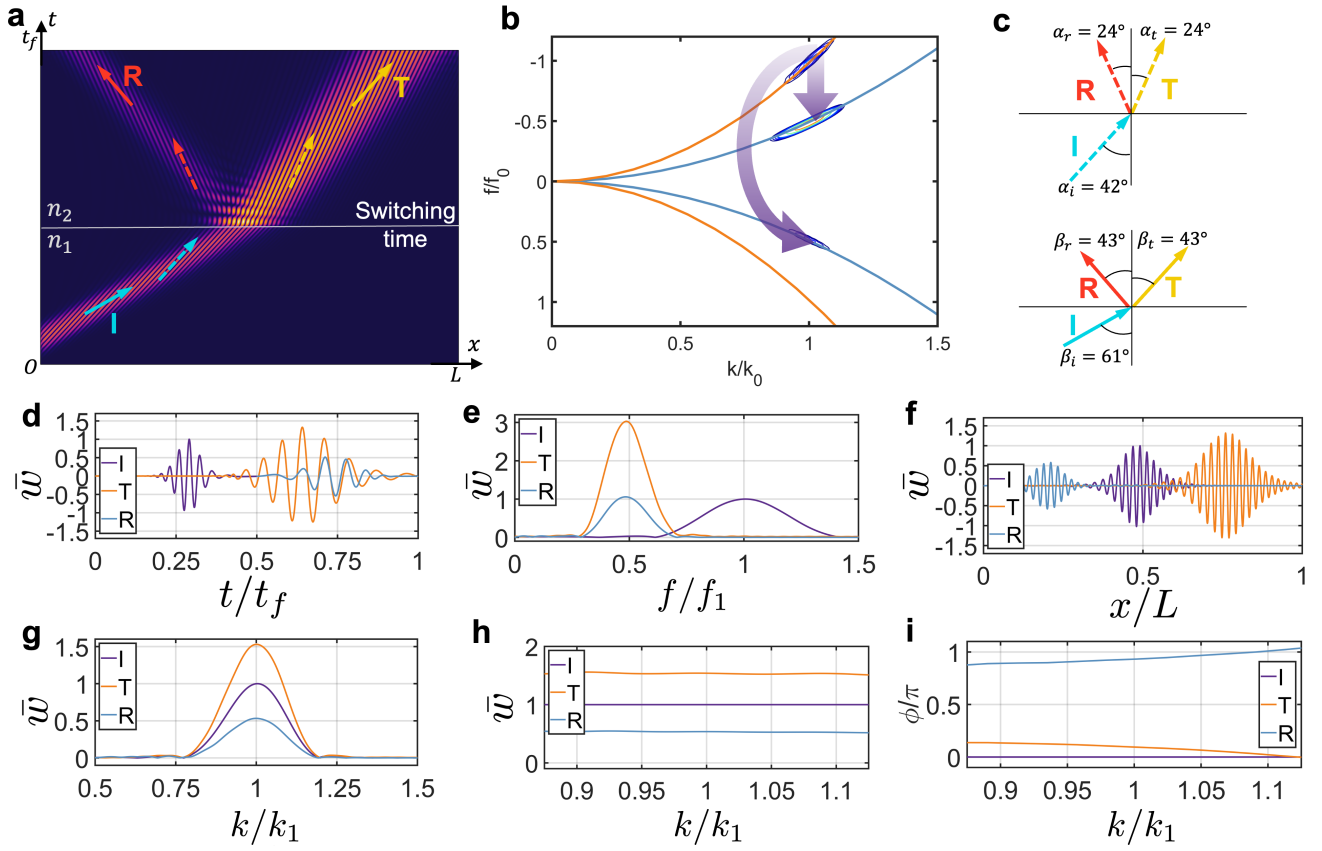


FIG. S7. **Numerical investigation of temporal refraction and reflection in a long metabeam.** **a** The refraction and reflection process of an incident wave packet, consisting of 5 cycles in the time domain, visualized in a spacetime diagram. Here,  $L = 2.56\text{ m}$  and  $t_f = 6\text{ ms}$ . **b** The dispersion curves of the medium before (orange) and after (blue) the switching event, overlaid with a background contour diagram obtained from a 2D Fourier transform of the spacetime data in **a**. **c** The angular relationship between the incident, reflected, and refracted waves for both a plane wave and a wave packet, with arrows translated from the spacetime diagram in **a**. **d** The incident (purple) and reflected (blue) signals measured at  $x = 0.28L$ , and the refracted signal (orange) observed at  $x = 0.62L$ . **e** The spectral analysis of the time-domain signals in **d**. **f** The incident spatial profile (purple) measured at  $t = 0.25t_f$ , along with the reflected and transmitted spatial profiles (blue and orange, respectively) measured at  $t = 0.75t_f$ . **g** The spectral analysis of the spatial-domain signals in **f**. **h** The normalized spectral data for the incident, reflected, and refracted waves in **g**, each normalized by the amplitude distribution of the incident wave. **i** The relationship between phase and wavenumber.

different wavenumbers, consistent with Eq. (9) of the main text.

## 5. REFRACTION AND REFLECTION AT A TIME INTERFACE FOR THE SWITCH FROM OFF TO ON IN EXPERIMENT

In this section, we examine temporal refraction and reflection during a switch transition from OFF to ON for an incident wave with a frequency of 6 kHz. The setup and parameters are identical to those in Fig. 2 of the main text. In this scenario, the refractive index ratio is  $n_1/n_0 = 1.17$ , and the impedance ratio is  $Z_1/Z_0 = 0.85$ . In Fig. S8a, the incident wave splits into a refracted wave and a reflected wave after passing through the time interface. In Fig. S8b, the incident angle of the plane waves is  $\alpha_i = 48^\circ$ , with refracted and reflected angles of  $\alpha_t = 43^\circ$  and  $\alpha_r = 43.5^\circ$ , respectively. The ratio  $\tan \alpha_t / \tan \alpha_i = 0.84$  closely matches the refractive index ratio  $n_1/n_2 = 0.85$ , validating Snell's law as described in Eq. (S12) of the main text.

A 2D Fourier transform is applied to the data in Fig. S8a, with the results shown in Fig. S8c. In Fig. S8b, the frequency of the incident wave shifts from  $f_0$  to  $0.83f_0$  and  $-0.83f_0$ , while the wavenumber remains constant. To further confirm the frequency conversion and wavenumber invariance, time-domain signals measured at  $x/L = 0.05$



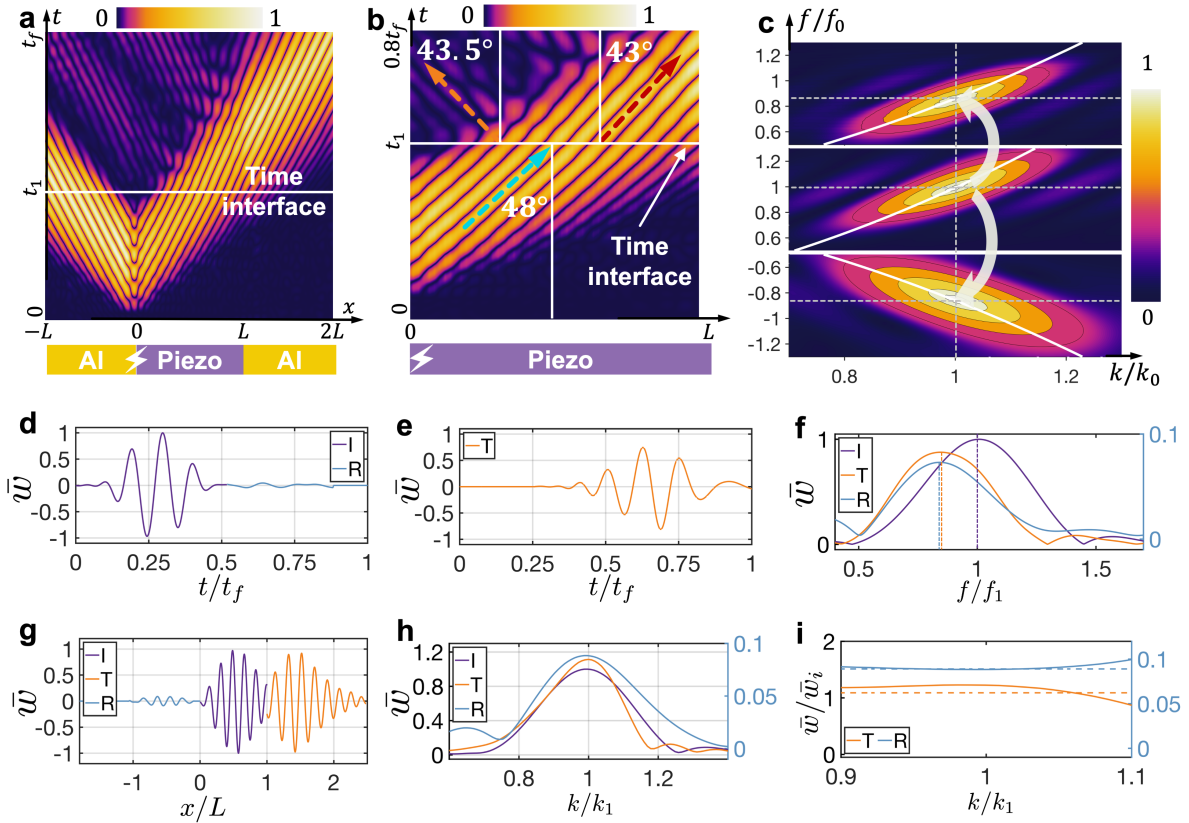


FIG. S8. **Temporal refraction and reflection in the metabeam with switch from OFF to ON.** **(a) (b)** The top panels show the simulation **(a)** and experiment **(b)** of wave scattering from an incident wave packet consisting of 3 cycles in the time domain, with  $t_f = 1.1$  ms and  $t_1 = 0.44$  ms, at a time interface in a spacetime diagram. The bottom panels depict the system, with  $L = 0.32$  m, composed of two aluminum beams (Al) and a piezo-metabeam (Piezo), with the excitation (lightning symbol) located at the left interface. **(c)** The 2D Fourier transform of the experimental data shown in **(b)**. **(d)** The incident (purple) and reflected (blue) signals measured at  $x = 0.05L$ . **(e)** The refracted signal (orange) observed at  $x = L$ . **(f)** The spectral analysis of the time-domain signals from **(d)** and **(e)**. **(g)** The incident spatial profile (purple) measured at  $t = 1/3t_f$ , along with the reflected and transmitted spatial profiles (blue and orange, respectively) at  $t = 2/3t_f$ . **(h)** The spectral analysis of the spatial-domain signals from **(g)**. **(i)** The normalized spectral data for the reflected and refracted waves in **(h)**, each normalized by the amplitude distribution of the incident wave.

and  $x/L = 1$  are shown in Fig. S8d,e, where three distinct wave packets corresponding to the incident, refracted, and reflected waves are clearly visible. The normalized frequencies  $f_t/f_0 = 0.83$  for the refracted wave and  $f_r/f_0 = 0.83$  for the reflected wave quantitatively confirm the frequency shift relative to the incident wave, as shown in Fig. S8f, indicating a breakdown of energy conservation. Additionally, the spatial-domain signals measured at  $t/t_f = 1/3$  and  $t/t_f = 2/3$  are shown in Fig. S8g. The central wavenumbers  $k_t$  for the refracted wave and  $k_r$  for the reflected wave are consistent with the central wavenumber  $k_1$  of the incident wave, as depicted in Fig. S8h, demonstrating the conservation of momentum. The normalized spectral data for the refracted and reflected waves is presented in Fig. S8i, where the normalized amplitudes are independent of the wavenumber and closely align with the theoretical predictions, thereby verifying the Fresnel equation in Eq. (9) of the main text.

## 6. REFRACTION AND REFLECTION AT A TIME INTERFACE FOR DIFFERENT FREQUENCIES IN THE EXPERIMENT

In this section, we examine wave refraction and reflection at different excitation frequencies, specifically 8 kHz (Fig. S9a-f) and 10 kHz (Fig. S9g-l), for switching transitions from ON to OFF and from OFF to ON, respectively. The excitation frequency refers to the frequency of the signal generated by the function generator, which may differ slightly from the incident frequency, defined as the peak position in the wave spectrum. The switching time in these cases is

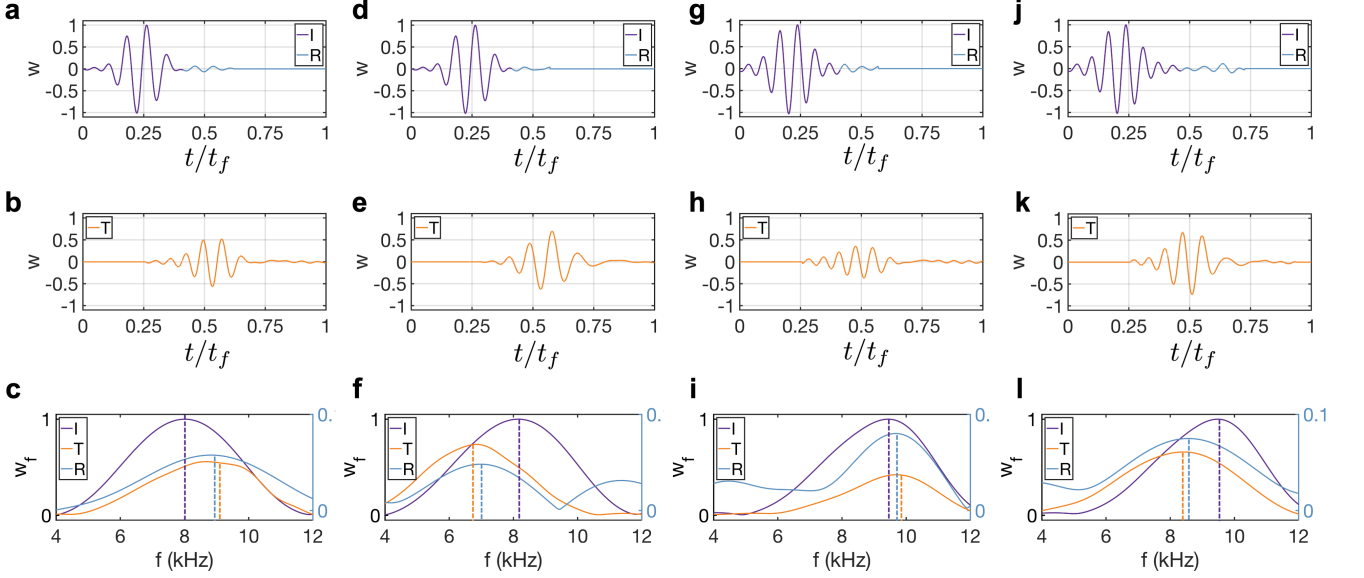


FIG. S9. **Spectral analysis of wave refraction and reflection at a time interface across different frequencies.** **a** (d) The incident temporal profile (purple) with an excitation frequency of 8 kHz, measured at  $t = 1/3t_f$ , and the reflected temporal profile (orange) at  $t = 2/3t_f$ . The switch transitions from ON to OFF (a) and from OFF to ON (d). **b** (e) The reflected and refracted temporal profiles (blue) at  $t = 2/3t_f$ . **c** (f) The spectral analysis of the incident, refracted, and reflected waves. **g** (j) The incident temporal profile (purple) with an excitation frequency of 10 kHz, measured at  $t = 1/3t_f$ , and the reflected temporal profile (orange) at  $t = 2/3t_f$ . The switch transitions from ON to OFF (g) and from OFF to ON (j). **h** (k) The reflected and refracted temporal profiles (blue) at  $t = 2/3t_f$ . **i** (l) The spectral analysis of the incident, refracted, and reflected waves.

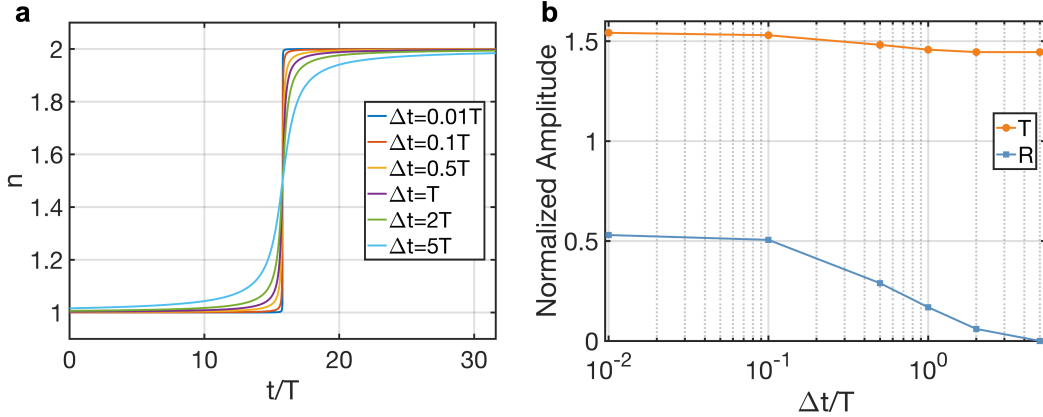


FIG. S10. **The effect of finite switching time.** **a** Different waveforms of  $n(t)$  with parameters  $\delta = 0.5$  and  $\alpha = 1$ . **b** Temporal refraction and reflection ratios as a function of  $\Delta t/T$ , where  $T$  is the period of the incident wave.

the same as that used for the case with an excitation frequency of 6 kHz.

As shown in Fig. S9c (f), the frequencies of the refracted and reflected waves shift from 8 kHz (incident wave) to 9 kHz and 7 kHz, respectively. In Fig. S9i (l), the frequencies of the refracted and reflected waves shift from 9.5 kHz (incident wave) to 9.8 kHz and 8.5 kHz, respectively.

For the 10 kHz case, the frequency shift does not satisfy Snell's law precisely. This discrepancy arises because the relatively high frequency leads to a smaller wavelength, increasing the ratio of the unit cell length to the wavelength. Consequently, the long-wave approximation is less valid, and the metabeam can no longer be considered a homogeneous beam. Furthermore, at higher frequencies, the homogeneous Euler-Bernoulli beam model becomes invalid, making the reflection and refraction less distinguishable and leading to inaccuracies in the frequency shift.

## 7. NUMERICAL INVESTIGATION OF THE EFFECT OF FINITE SWITCHING TIME

In the experiment, the switch does not transition instantaneously between states. In this section, we analyze the effect of finite switching time on the amplitudes of the refracted and reflected waves. To study this, various smooth time boundaries are modeled using the analytical function  $n(t) = \frac{\Delta n}{\pi} \arctan\left(\frac{t-t_c}{\Delta t}\right) + n_0 + \frac{\Delta n}{2}$ , where  $n_0$  and  $\Delta n = n_0$  represent the initial and changed refractive indices, and  $\Delta t/T$  determines the sharpness of the waveform. Here,  $T$  is the period of the incident wave.

In Fig. S10a, the smooth step function is displayed for different values of  $\Delta t/T$ . The corresponding normalized amplitudes of the refracted and reflected waves, relative to the incident wave, are shown in Fig. S10b. The numerical setup in this section is the same as that described in Part B of Supplementary Section IV. When  $\Delta t/T$  is very small (less than 0.1), the amplitudes of both the refracted and reflected waves remain constant and closely align with the theoretical predictions from Fresnel's formula. As long as  $\Delta t/T$  stays within this range, the time interface can be regarded as ideal. In our experiment,  $\Delta t/T = 0.001$ , which is much smaller than 0.1, confirming that the interface behaves as an ideal time interface.

If  $\Delta t/T$  exceeds 0.1, the amplitudes of both the refracted and reflected waves decrease as  $\Delta t/T$  increases. However, the amplitude of the refracted wave approaches a finite value of  $\sqrt{2}$ , while the amplitude of the reflected wave diminishes to zero. This indicates that no reflected wave is generated when the refractive index changes very gradually. This behavior can be explained by the adiabatic theorem, which states that a system will remain in the same eigenstate if its parameters vary slowly enough. In the adiabatic limit, the wave's evolution can be described by [2, 3]:

$$w(x, t) = \frac{A_i}{\sqrt{\omega(t)}} e^{ikx - \int_{t_0}^t \omega(t') dt'}. \quad (\text{S2})$$

In this scenario, the wave remains a right-propagating wave, with its amplitude and frequency gradually changing over time and no reflected wave being generated. Since the ratio of the final frequency to the initial frequency is  $\sqrt{2}$ , the normalized amplitude of the refracted wave becomes  $\sqrt{2}$ , consistent with the results shown in Fig. S10b. Between the sudden-change limit and the adiabatic limit, the normalized amplitudes vary continuously as  $\Delta t/T$  increases, falling within the range defined by these two extremes.

## 8. NUMERICAL STUDY OF TEMPORAL REFRACTION AND REFLECTION OF AN ASYMMETRIC PULSE

In this section, we demonstrate that the observed reflection is a temporal reflection rather than a spatial one. To highlight this distinction, we consider the scattering of an asymmetric pulse at a temporal interface. The simulation setup is identical to that described in Supplementary Section 4B. As shown in Fig. S11a, the spacetime diagram captures the behavior of the pulse upon encountering the interface.

Key differences between spatial and temporal reflections are evident in the order of pulse peaks. For spatial reflection, the higher peak of the incident pulse appears first, followed by the lower peak. In contrast, temporal reflection reverses this order: the lower peak arrives first, and the higher peak follows. This reversal in the time domain is shown in the normalized signals in Fig. S11b. Here, the incident ( $\bar{w}_i$ ) and reflected ( $\bar{w}_r$ ) signals, measured at  $x/L = 0.3$ , clearly demonstrate this inversion. In the spatial domain, the incident waves are shown in Fig. S11c. Fig. S11d displays the refracted ( $\bar{w}_t$ ) and reflected ( $\bar{w}_r$ ) signals, which are normalized and measured at  $t/t_f = 0.3$ . The reflected wave packet with the smaller peak appears first, followed by the reflected wave packet with the larger peak, which is opposite to the order observed in spatial reflection.

## 9. DERIVATION OF TEMPORAL CONTINUITY CONDITIONS

The equation of motion for the Euler-Bernoulli beam is given by:

$$\partial_t p = \partial_{xx} M + q(t), \quad (\text{S3})$$

where  $p = \rho A \partial_t w$  represents the momentum,  $M$  is the bending moment, and  $q$  is a time dependent external force. Meanwhile, the bending curvature  $\kappa$  is defined as

$$\kappa = \partial_{xx} w. \quad (\text{S4})$$

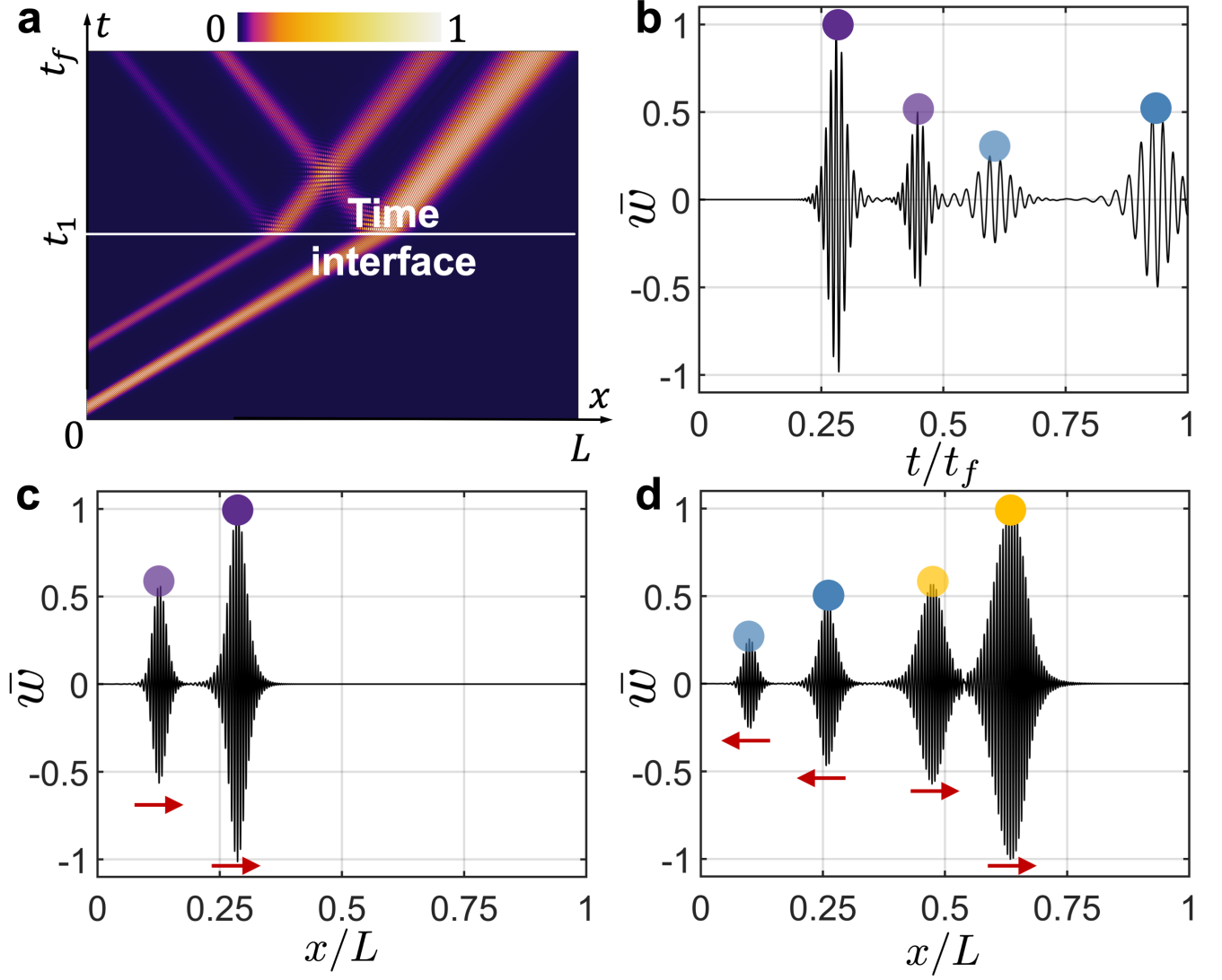


FIG. S11. **Refraction and reflection of an asymmetric pulse at a time interface.** **a** The spacetime diagram of a simulated asymmetric pulse scattering at a temporal interface. **b** The normalized incident ( $\bar{w}_i$ ) and reflected ( $\bar{w}_r$ ) signals measured at  $x/L = 0.3$ . The purple wave packet represents the incident wave with a higher amplitude, while the light purple wave packet corresponds to the incident wave with a lower amplitude. Similarly, the blue wave packet represents the reflected wave generated by the higher-amplitude incident wave, and the light blue wave packet corresponds to the reflected wave generated by the lower-amplitude incident wave. **c** The normalized incident ( $\bar{w}_i$ ) signal measured at  $t/t_f = 0.3$ . The purple wave packet represents the incident wave with a higher amplitude, while the light purple wave packet corresponds to the incident wave with a lower amplitude. **d** The normalized refracted ( $\bar{w}_t$ ) and reflected ( $\bar{w}_r$ ) signals measured at  $t/t_f = 0.3$ . The orange wave packet represents the refracted wave with a higher amplitude, while the light orange wave packet corresponds to the incident wave with a lower amplitude. Similarly, the blue wave packet represents the reflected wave generated by the higher-amplitude incident wave, and the light blue wave packet corresponds to the reflected wave generated by the lower-amplitude incident wave.

The bending momentum and bending curvature satisfy the constitutive relation

$$M = -D(t)\kappa. \quad (\text{S5})$$

where  $D(t) = E(t)I$  is the time-dependent bending stiffness,  $E(t)$  is the time-dependent Young's modulus, and  $I$  is the second moment of area. Substituting Eq. (S5) and Eq. (S4) into the equation of motion (Eq. (S3)) yields the governing equations for the Euler-Bernoulli beam, as presented in Eq. (1) of the main text

$$\frac{\partial}{\partial t} \left( \rho A \frac{\partial w(x,t)}{\partial t} \right) + \frac{\partial^2}{\partial x^2} \left( D(t) \frac{\partial^2 w(x,t)}{\partial x^2} \right) = q(t). \quad (\text{S6})$$

Integrating Eq. (S6) from initial time  $t'$  to an arbitrary time  $t$  gives

$$\rho A \frac{\partial w(x, t)}{\partial t} \Big|_{t'}^t + \int_{t'}^t dt D(t) \frac{\partial^4 w(x, t)}{\partial x^4} = \int_{t'}^t q(t) dt. \quad (\text{S7})$$

Taking  $t' = t_1^- = t_1 - \epsilon$  to  $t = t_1^+ = t_1 + \epsilon$  with a  $\epsilon \rightarrow 0^+$ , we expect that the second term in Eq. (S7) is zero, due to the finite values of fields. The term on the right-hand side represents the impulse, which is not considered in our study and is therefore set to zero. Then, we obtain the first temporal boundary condition that describes the continuity of momentum:

$$\rho A \frac{\partial w}{\partial t} \Big|_{t=t_1^+} = \rho A \frac{\partial w}{\partial t} \Big|_{t=t_1^-}. \quad (\text{S8})$$

Since the density is time-independent, Eq. (S8) implies the continuity of velocity

$$\frac{\partial w}{\partial t} \Big|_{t=t_1^+} = \frac{\partial w}{\partial t} \Big|_{t=t_1^-}. \quad (\text{S9})$$

Similarly, integrating Eq. (S7) from  $t_1^-$  to  $t_1^+$  as  $\epsilon \rightarrow 0^+$  with respect to  $t$  without the impulse gives the second temporal boundary condition that describes the continuity of displacement:

$$w|_{t=t_1^+} = w|_{t=t_1^-}. \quad (\text{S10})$$

## 10. RELATIONSHIP BETWEEN THE ANGLES OF INCIDENCE AND REFRACTION

In the main text, the Snell's law is written as

$$\omega_1 n_1 = \omega_0 n_0. \quad (\text{S11})$$

The more familiar form describing the geometric relationship between the angles of the incident and refracted waves in a space-time diagram is presented as follows.

In the  $(x, ct)$  space, where  $c$  is a reference speed to maintain dimensional consistency, the angle  $\alpha$  between the propagation direction of a plane wave (with phase velocity  $\omega/k$ ) and the time axis satisfies the relation  $\tan \alpha = \omega/(kc) = k/(nc)$ . This results in the geometric relationship between the angle of incidence and the angle of refraction:

$$\frac{\tan \alpha_0}{\tan \alpha_1} = \frac{n_1}{n_0}. \quad (\text{S12})$$

Eq. (S12) can be interpreted as the temporal Snell's law, describing the geometric relationship between the angles of the incident and refracted waves in a space-time diagram. This is analogous to the traditional Snell's law, which applies to wave propagation in two-dimensional space.

The dispersion relation of flexural waves is a quadratic function, making them dispersive, meaning the propagation direction of a wave packet differs from that of a plane wave. We now explore the geometric relationship between the incident and refracted angles of the wave packet. The angle between the propagation direction of the wave packet and the time axis is defined as  $\tan \beta = v_g/c$ , where the group velocity  $v_g = d\omega/dk = 2k\sqrt{D/\rho A} = 2k/n$ . Therefore, the geometric relationship between the incident and refracted angles of the wave packet is

$$\frac{\tan \beta_0}{\tan \beta_1} = \frac{n_1}{n_0}. \quad (\text{S13})$$

Interestingly, this relationship is the same as the temporal Snell's law for plane waves.

Fig. S12 shows the relationship between the angles of incidence and refraction in a space-time diagram. Here, the angle of the incident plane wave  $\alpha_i$ , the angle of the refracted plane wave  $\alpha_t$ , and the angle of the reflected plane wave  $\alpha_r$  are  $49^\circ$ ,  $52^\circ$ , and  $52.5^\circ$ , respectively. The ratios  $\tan \alpha_i / \tan \alpha_t = 0.9$  and  $\tan \alpha_i / \tan \alpha_r = 0.88$  are close to the refractive index ratio  $n_1/n_0 = 0.85$ , confirming the temporal Snell's law in Eq. (S12). The geometric relation of the wave packet in Eq. (S13) is verified in a longer metabeam using 5-cycle tone-burst excitation, as detailed in [Supplementary Section 4B](#).

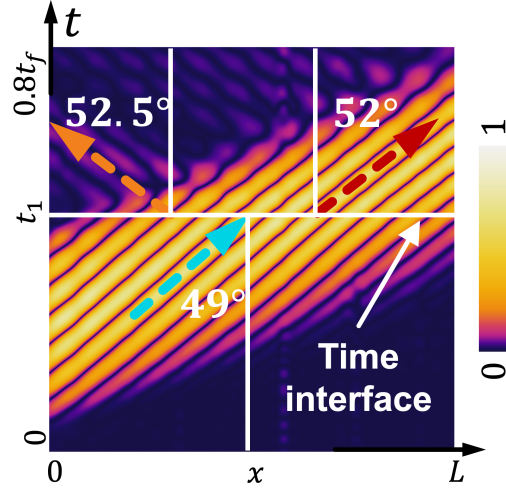


FIG. S12. Relationship between the angles of incidence, refraction, and reflection.

## 11. NOETHER'S THEOREM AND CONSERVATION LAWS

### A. Complex scalar field theory for the Euler-Bernoulli beam

As we know, when a flexural incident wave encounters an interface where the refractive index of the beam changes abruptly, it splits into a refracted wave and a reflected wave, as shown in Fig. S13a,b. Remarkably, the governing equation of the Euler-Bernoulli beam model inherently supports space-time duality, implying temporal analogs of reflection and refraction when a flexural wave encounters a time boundary, as illustrated in Fig. S13c,d. Wave scattering at both spatial and temporal boundaries adheres to Noether's theorem, which reveals the fundamental connection between the symmetries of a physical system and its conservation laws. In systems with abrupt spatial changes, the breakdown of space translation invariance leads to the non-conservation of momentum. However, the system remains invariant in the time direction, preserving time translation invariance and, consequently, the conservation of energy. In this section, energy and momentum are derived as Noether's charges in accordance with Noether's theorem.

In this paper, we examine wave propagation in the frequency domain, which involves complex analysis. There are two methods for deriving Noether's charge. The first method involves obtaining the expression for Noether's charge using real scalar field theory, followed by applying a periodic average to derive the corresponding charge in the complex domain [4, 5]. The second method derives the expression for Noether's charge directly from complex scalar field theory, avoiding time averaging. In this study, we employ the second method.

The complex scalar field is defined as  $w(x, t) = [w_r(x, t) + iw_i(x, t)]/\sqrt{2}$ , constructed from two identical real fields,  $w_r(x, t)$  and  $w_i(x, t)$  [6–8]. For convenience, we use  $w(x, t)$  and  $w^\dagger(x, t)$  as independent variables instead of  $w_r(x, t)$  and  $w_i(x, t)$ . The Lagrangian for the Euler-Bernoulli beam can be extended from that of real scalar field theory [9] as follows:

$$\mathcal{L} = \frac{1}{2}\rho A \partial_t w^\dagger(x, t) \partial_t w(x, t) - \frac{1}{2}EI \partial_{xx} w^\dagger(x, t) \partial_{xx} w(x, t) \quad (\text{S14})$$

And the action  $S$ , the time integral of the Lagrangian  $\mathcal{L}$ , can be written as

$$S = \int \mathcal{L} dt = \int \mathcal{L} \left( w_t, w_t^\dagger, w_{xx}, w_{xx}^\dagger \right) dx dt \quad (\text{S15})$$

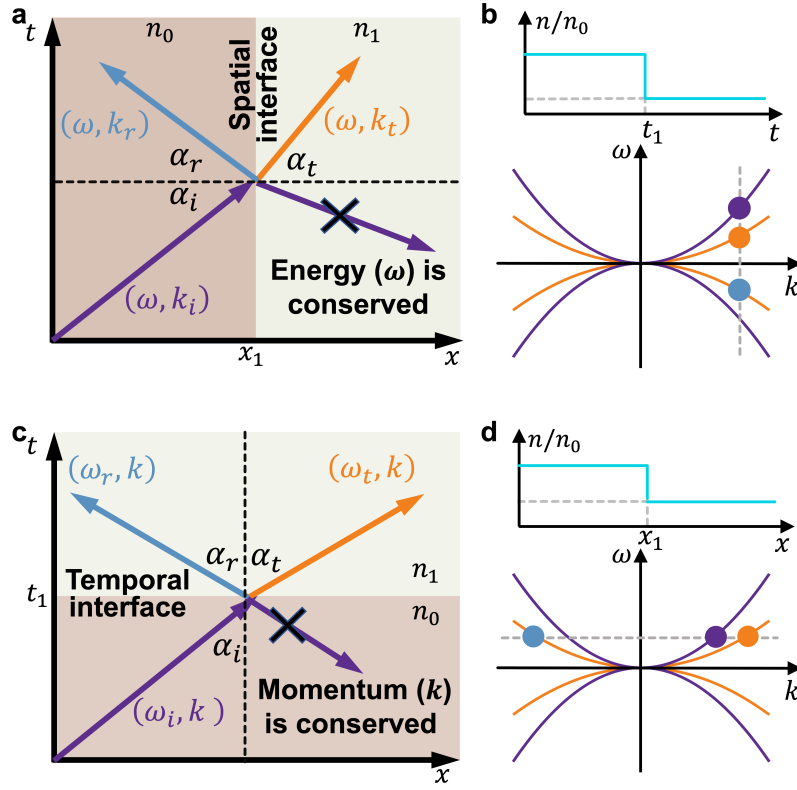


FIG. S13. **Refraction and reflection of flexural waves at a time interface.** (a) (c) Spacetime diagram of wave refraction and reflection at a spatial (temporal) interface. The subscripts  $i$ ,  $r$ , and  $t$  correspond to the incident, reflected, and refracted waves, respectively. (b) (d) The top panel shows the index of refraction versus  $x(t)$ , with an abrupt change at  $x_1(t_1)$ . The bottom panel displays the dispersion curves: the medium before (after)  $x_1(t_1)$  is represented by a purple (orange) solid line. The blue, red, and yellow points correspond to the incident, reflected, and refracted waves, respectively.

The principle of least action states [6]

$$0 = \delta S$$

$$\begin{aligned}
&= \int dxdt \left\{ \frac{\partial \mathcal{L}}{\partial (\partial_t w)} \delta (\partial_t w) + \frac{\partial \mathcal{L}}{\partial (\partial_{xx} w)} \delta (\partial_{xx} w) + \frac{\partial \mathcal{L}}{\partial (\partial_t w^\dagger)} \delta (\partial_t w^\dagger) + \frac{\partial \mathcal{L}}{\partial (\partial_{xx} w^\dagger)} \delta (\partial_{xx} w^\dagger) \right\} \\
&= \int dxdt \left\{ \partial_t \left( \frac{\partial \mathcal{L}}{\partial (\partial_t w)} \delta w \right) - \partial_t \left( \frac{\partial \mathcal{L}}{\partial (\partial_t w)} \right) \delta w + \partial_x \left( \frac{\partial \mathcal{L}}{\partial (\partial_{xx} w)} \partial_x \delta w \right) - \partial_x \left( \partial_x \frac{\partial \mathcal{L}}{\partial (\partial_{xx} w)} \delta w \right) + \partial_{xx} \left( \frac{\partial \mathcal{L}}{\partial (\partial_{xx} w)} \right) \delta w \right. \\
&\quad \left. + \partial_t \left( \frac{\partial \mathcal{L}}{\partial (\partial_t w^\dagger)} \delta w^\dagger \right) - \partial_t \left( \frac{\partial \mathcal{L}}{\partial (\partial_t w^\dagger)} \right) \delta w^\dagger + \partial_x \left( \frac{\partial \mathcal{L}}{\partial (\partial_{xx} w^\dagger)} \partial_x \delta w^\dagger \right) - \partial_x \left( \partial_x \frac{\partial \mathcal{L}}{\partial (\partial_{xx} w^\dagger)} \delta w^\dagger \right) + \partial_{xx} \left( \frac{\partial \mathcal{L}}{\partial (\partial_{xx} w^\dagger)} \right) \delta w^\dagger \right\} \\
&= \int dxdt \left\{ -\partial_t \left( \frac{\partial \mathcal{L}}{\partial (\partial_t w)} \right) \delta w + \partial_{xx} \left( \frac{\partial \mathcal{L}}{\partial (\partial_{xx} w)} \right) \delta w - \partial_t \left( \frac{\partial \mathcal{L}}{\partial (\partial_t w^\dagger)} \right) \delta w^\dagger + \partial_{xx} \left( \frac{\partial \mathcal{L}}{\partial (\partial_{xx} w^\dagger)} \right) \delta w^\dagger \right\}
\end{aligned} \tag{S16}$$

where the rules of variational operations can be found in [10]. By factoring out  $\delta w$  ( $\delta w^\dagger$ ) from the first two terms (last two terms), we note that, since the integral must vanish for arbitrary  $\delta w$  ( $\delta w^\dagger$ ), the quantity multiplying  $\delta w$  ( $\delta w^\dagger$ ) must also vanish at all points. This leads us to the Euler-Lagrange equation of motion for the complex field:

$$\partial_t \left( \frac{\partial \mathcal{L}}{\partial (\partial_t w)} \right) - \partial_{xx} \left( \frac{\partial \mathcal{L}}{\partial (\partial_{xx} w)} \right) = 0 \tag{S17}$$

$$\partial_t \left( \frac{\partial \mathcal{L}}{\partial (\partial_t w^\dagger)} \right) - \partial_{xx} \left( \frac{\partial \mathcal{L}}{\partial (\partial_{xx} w^\dagger)} \right) = 0. \tag{S18}$$

### B. Time translation symmetry and energy conservation

We can describe the infinitesimal translation of time as

$$t \rightarrow t + \delta t \quad (\text{S19})$$

alternatively as a transformation of the field configuration

$$\begin{aligned} w(x, t) &\rightarrow w(x, t) = w(x, t) + \delta t \partial_t w(x, t), \\ w^\dagger(x, t) &\rightarrow w^\dagger(x, t) = w^\dagger(x, t) + \delta t \partial_t w^\dagger(x, t). \end{aligned} \quad (\text{S20})$$

More generally, we can allow the action to change by a surface term, since the presence of such a term would not affect our derivation of the Euler-Lagrange equations of motion Eq. (S17, S18). The Lagrangian, therefore, must be invariant under Eq. (S19) up to a divergence:

$$\mathcal{L} \rightarrow \mathcal{L} + \delta t \partial_t \mathcal{L}. \quad (\text{S21})$$

On the other hand, the change in the Lagrangian density  $\mathcal{L}$  is then given by

$$\begin{aligned} \delta \mathcal{L} &= \frac{\partial \mathcal{L}}{\partial (\partial_t w)} \delta (\partial_t w) + \frac{\partial \mathcal{L}}{\partial (\partial_t w^\dagger)} \delta (\partial_t w^\dagger) + \frac{\partial \mathcal{L}}{\partial (\partial_{xx} w)} \delta (\partial_{xx} w) + \frac{\partial \mathcal{L}}{\partial (\partial_{xx} w^\dagger)} \delta (\partial_{xx} w^\dagger) \\ &= \frac{\partial \mathcal{L}}{\partial (\partial_t w)} \partial_t (\delta w) + \frac{\partial \mathcal{L}}{\partial (\partial_t w^\dagger)} \partial_t (\delta w^\dagger) + \frac{\partial \mathcal{L}}{\partial (\partial_{xx} w)} \partial_{xx} (\delta w) + \frac{\partial \mathcal{L}}{\partial (\partial_{xx} w^\dagger)} \partial_{xx} (\delta w^\dagger) \\ &= \delta t \left[ \frac{\partial \mathcal{L}}{\partial (\partial_t w)} \partial_t (w_t) + \frac{\partial \mathcal{L}}{\partial (\partial_t w^\dagger)} \partial_t (w_t^\dagger) + \frac{\partial \mathcal{L}}{\partial (\partial_{xx} w)} \partial_{xx} (w_t) + \frac{\partial \mathcal{L}}{\partial (\partial_{xx} w^\dagger)} \partial_{xx} (w_t^\dagger) \right] \end{aligned} \quad (\text{S22})$$

Multiplying Eq. (S17) with  $\delta t w_t$  and Eq. (S18) with  $\delta t w_t^\dagger$ , and adding them into Eq. (S22) gives

$$\begin{aligned} \delta \mathcal{L} &= \delta t \partial_t \left( \frac{\partial \mathcal{L}}{\partial (\partial_t w)} w_t + \frac{\partial \mathcal{L}}{\partial (\partial_t w^\dagger)} w_t^\dagger \right) \\ &\quad + \delta t \partial_x \left[ \partial_x \left( \frac{\partial \mathcal{L}}{\partial (\partial_{xx} w)} \right) w_t + \partial_x \left( \frac{\partial \mathcal{L}}{\partial (\partial_{xx} w^\dagger)} \right) w_t^\dagger + \frac{\partial \mathcal{L}}{\partial (\partial_{xx} w)} w_{xt} + \frac{\partial \mathcal{L}}{\partial (\partial_{xx} w^\dagger)} w_{xt}^\dagger \right] \end{aligned} \quad (\text{S23})$$

The Lagrangian density  $\mathcal{L}$  could very well change by a divergence  $\delta \mathcal{L} = \delta t \partial_t \mathcal{L}$ . Therefore, the combination of Eq. (S23) and Eq. (S21) upon arbitrary infinitesimal time translation  $\delta t$  leads to

$$\partial_t j^{tt} + \partial_x j^{tx} = 0, \quad (\text{S24})$$

where

$$\begin{aligned} j^{tt} &= \frac{\partial \mathcal{L}}{\partial (\partial_t w)} w_t + \frac{\partial \mathcal{L}}{\partial (\partial_t w^\dagger)} w_t^\dagger - \mathcal{L} \\ j^{tx} &= \partial_x \left( \frac{\partial \mathcal{L}}{\partial (\partial_{xx} w)} \right) w_t + \partial_x \left( \frac{\partial \mathcal{L}}{\partial (\partial_{xx} w^\dagger)} \right) w_t^\dagger + \frac{\partial \mathcal{L}}{\partial (\partial_{xx} w)} w_{xt} + \frac{\partial \mathcal{L}}{\partial (\partial_{xx} w^\dagger)} w_{xt}^\dagger \end{aligned} \quad (\text{S25})$$

Then, performing the integration over  $x$  at constant time gives

$$\partial_t \int j^{tt} dx = 0, \quad (\text{S26})$$

where  $\int \partial_x j^{tx} dx = 0$  is used because this will vanish if the line is long enough [8]. Now we define  $\mathcal{H}$  as the energy density:

$$\mathcal{H} = \frac{\partial \mathcal{L}}{\partial (\partial_t w)} \partial_t w + \frac{\partial \mathcal{L}}{\partial (\partial_t w^\dagger)} \partial_t w^\dagger - \mathcal{L} \quad (\text{S27})$$

And the Hamiltonian (energy)

$$H = \int \mathcal{H} dx = \int dx \left( \frac{1}{2} \rho A \partial_t w^\dagger(x, t) \partial_t w(x, t) + \frac{1}{2} EI \partial_{xx} w^\dagger(x, t) \partial_{xx} w(x, t) \right). \quad (\text{S28})$$



is conserved for system with time translation symmetry according to Eq. (S26). The energy before the switching event is

$$H_0 = \left( \frac{1}{2} \rho A \omega_0^2 + \frac{1}{2} E_0 I_0 k_0^4 \right) A_i^2 = \frac{1}{Z_0^2} \rho A A_i^2, \quad (\text{S29})$$

whereas the energy density after the switching event is

$$H_1 = \left( \frac{1}{2} \rho A \omega_1^2 + \frac{1}{2} E_1 I_1 k_1^4 \right) (T^2 + R^2) A_i^2 = \frac{Z_0^2 + Z_1^2}{2Z_1^4} \rho A A_i^2 = \frac{Z_0^4 + Z_0^2 Z_1^2}{2Z_1^4} H_0, \quad (\text{S30})$$

where Eq. (9) in the main text is used. Now we can be easily verified that the energy in Eq. (S30) is not conserved:

$$H_1 \neq H_0 \quad (\text{S31})$$

for temporal media with  $Z_0 \neq Z_1$ . We conclude that the breaking of time translation symmetry leads to the breakdown of the conservation of energy.

### C. Space translation symmetry and momentum conservation

We can describe the infinitesimal translation of time as

$$x \rightarrow x + \delta x \quad (\text{S32})$$

alternatively as a transformation of the field configuration

$$\begin{aligned} w(x, t) &\rightarrow w(x, t) = w(x, t) + \delta x \partial_x w(x, t), \\ w^\dagger(x, t) &\rightarrow w^\dagger(x, t) = w^\dagger(x, t) + \delta x \partial_x w^\dagger(x, t). \end{aligned} \quad (\text{S33})$$

More generally, we can allow the action to change by a surface term, since the presence of such a term would not affect our derivation of the Euler-Lagrange equations of motion Eq. (S17, S18). The Lagrangian, therefore, must be invariant under Eq. (S32) up to a divergence:

$$\mathcal{L} \rightarrow \mathcal{L} + \delta x \partial_x \mathcal{L}. \quad (\text{S34})$$

On the other hand, the change in the Lagrangian density  $\mathcal{L}$  is then given by

$$\begin{aligned} \delta \mathcal{L} &= \frac{\partial \mathcal{L}}{\partial (\partial_t w)} \delta (\partial_t w) + \frac{\partial \mathcal{L}}{\partial (\partial_t w^\dagger)} \delta (\partial_t w^\dagger) + \frac{\partial \mathcal{L}}{\partial (\partial_{xx} w)} \delta (\partial_{xx} w) + \frac{\partial \mathcal{L}}{\partial (\partial_{xx} w^\dagger)} \delta (\partial_{xx} w^\dagger) \\ &= \delta x \left[ \frac{\partial \mathcal{L}}{\partial (\partial_t w)} \partial_t (w_x) + \frac{\partial \mathcal{L}}{\partial (\partial_t w^\dagger)} \partial_t (w_x^\dagger) + \frac{\partial \mathcal{L}}{\partial (\partial_{xx} w)} \partial_{xx} (w_x) + \frac{\partial \mathcal{L}}{\partial (\partial_{xx} w^\dagger)} \partial_{xx} (w_x^\dagger) \right] \end{aligned} \quad (\text{S35})$$

Multiplying Eq. (S17) with  $\delta x w_x$  and Eq. (S18) with  $\delta x w_x^\dagger$ , and adding them into Eq. (S35) gives

$$\begin{aligned} \delta \mathcal{L} &= \delta x \partial_t \left( \frac{\partial \mathcal{L}}{\partial (\partial_t w)} w_x + \frac{\partial \mathcal{L}}{\partial (\partial_t w^\dagger)} w_x^\dagger \right) \\ &+ \delta x \partial_x \left[ \partial_x \left( \frac{\partial \mathcal{L}}{\partial (\partial_{xx} w)} \right) w_x + \partial_x \left( \frac{\partial \mathcal{L}}{\partial (\partial_{xx} w^\dagger)} \right) w_x^\dagger + \frac{\partial \mathcal{L}}{\partial (\partial_{xx} w)} w_{xx} + \frac{\partial \mathcal{L}}{\partial (\partial_{xx} w^\dagger)} w_{xx}^\dagger \right] \end{aligned} \quad (\text{S36})$$

The Lagrangian density  $\mathcal{L}$  may change by a divergence,  $\delta \mathcal{L} = \delta x \partial_x \mathcal{L}$ . Therefore, combining Eq. (S35) and Eq. (S34) under an arbitrary infinitesimal time translation  $\delta x$  results in the following expression:

$$\partial_t j^{tx} + \partial_x j^{xx} = 0, \quad (\text{S37})$$

where

$$\begin{aligned} j^{tx} &= \frac{\partial \mathcal{L}}{\partial (\partial_t w)} w_x + \frac{\partial \mathcal{L}}{\partial (\partial_t w^\dagger)} w_x^\dagger \\ j^{xx} &= \partial_x \left( \frac{\partial \mathcal{L}}{\partial (\partial_{xx} w)} \right) w_x + \partial_x \left( \frac{\partial \mathcal{L}}{\partial (\partial_{xx} w^\dagger)} \right) w_x^\dagger + \frac{\partial \mathcal{L}}{\partial (\partial_{xx} w)} w_{xx} + \frac{\partial \mathcal{L}}{\partial (\partial_{xx} w^\dagger)} w_{xx}^\dagger \end{aligned} \quad (\text{S38})$$

Then, performing the integration over  $x$  at constant time gives

$$\partial_t \int j^{tx} dx = 0, \quad (\text{S39})$$

where  $\int \partial_x j^{xx} dx = 0$  is used because this will vanish if the line is long enough [8]. Now we define  $p$  as the momentum density:

$$p = j^{tx} = \frac{\partial \mathcal{L}}{\partial (\partial_t w)} \partial_x w + \frac{\partial \mathcal{L}}{\partial (\partial_t w^\dagger)} \partial_x w^\dagger \quad (\text{S40})$$

The conserved charges (momentum) associated with spatial translations are

$$P = \int p dx = \int dx \rho A [(\partial_t w^\dagger) w_x + (\partial_t w) w_x^\dagger]. \quad (\text{S41})$$

The momentum of the wave before the switching event is

$$P_0 = 2\rho A \omega_0 k_0 A_i^2, \quad (\text{S42})$$

whereas the momentum of waves after the switching event is

$$P_1 = 2\rho A \omega_1 k_1 (T^2 - R^2) A_i^2. \quad (\text{S43})$$

With the aid of Eq. (9) in the main text, the momentum conservation can be easily verified that

$$P_0 = P_1 = 2Z_0 k_0^3 A_i^2. \quad (\text{S44})$$

## 12. OPTIMIZATION METHOD FOR BROADBAND ANTI-REFLECTION AND WAVE AMPLIFICATION AT MULTIPLE TIME INTERFACES

In this section, we provide a detailed description of the optimization problem for designing temporal multilayer media aimed at eliminating broadband reflected waves and enhancing wave amplification.

For single-frequency reflected wave elimination, the optimization problem can be proposed as

$$\begin{aligned} & \underset{n_1, t_2}{\text{minimize}} && |R(n_1, t_2, f_0 = 6 \text{ kHz})|^2 \\ & \text{subject to} && n_0 \leq n_1 \leq 2n_0, \\ & && \Delta t_1 > 0 \end{aligned} \quad (\text{S45})$$

For broadband reflected wave elimination, the optimization problem can be proposed as

$$\begin{aligned} & \underset{\mathbf{n}, \mathbf{t}}{\text{minimize}} && \int_{f_a}^{f_b} |R(\mathbf{n}, \mathbf{t}, f_0)|^2 df_0 \\ & \text{subject to} && \min(n_0, n_{M+1}) \leq n_i \leq \max(n_0, n_{M+1}), \quad i = 1, \dots, M \\ & && \Delta t_j > 0, \quad j = 1, \dots, M \end{aligned} \quad (\text{S46})$$

where  $f_a = 0.5f_0$ ,  $f_b = 1.5f_0$ ,  $M = 4$ ,  $n_{M+1} = 2n_0$ .

For wave amplification, the optimization problem can be proposed as

$$\begin{aligned} & \underset{\mathbf{n}, \mathbf{t}}{\text{minimize}} && -|T(\mathbf{n}, \mathbf{t}, f_0 = 6 \text{ kHz})|^2 \\ & \text{subject to} && 0 \leq n_i \leq 3n_0, \quad i = 1, \dots, M \\ & && \Delta t_j > 0, \quad j = 1, \dots, M \end{aligned} \quad (\text{S47})$$

where  $T(\mathbf{n}, \mathbf{t})$  is the refraction coefficient,  $M = 3$ ,  $n_{M+1} = n_0$ .

The constrained nonlinear optimization problem is solved numerically by calling the MATLAB function "fmincon" with given random initial conditions satisfying the constraints, where the sequential quadratic programming (SQP) algorithm is implemented.

### 13. RESISTOR FUNCTIONS IN SMART WAVEFORM MORPHING AND INFORMATION

In the main text, the transfer functions can be modulated into various forms, such as sinusoidal functions and smooth step functions for smart waveform morphing and information coding. The sinusoidal function of the resistor in Fig. 6b of the main text is

$$R_1(t) = 5.1 + 0.1 \cos \frac{2\pi t}{T} \quad (\text{S48})$$

where  $T = 0.2$  s. The smooth step function of the resistor in Fig. 6e of the main text is

$$R_1(t) = \begin{cases} 5.2 & 0 \leq t \leq \frac{T-\Delta T}{2} \\ 0.2 \times \frac{t-mT/2+\Delta T/2}{\Delta T} + 5.2 & \frac{mT-\Delta T}{2} \leq t \leq \frac{mT+\Delta T}{2} \\ 5.4 & \frac{mT+\Delta T}{2} \leq t \leq mT - \frac{\Delta T}{2} \\ -0.2 \times \frac{t-mT+\Delta T/2}{\Delta T} + 5.4 & mT - \frac{\Delta T}{2} \leq t \leq mT + \frac{\Delta T}{2} \\ 5.2 & mT + \frac{\Delta T}{2} \leq t \leq \frac{3mT}{2} - \frac{\Delta T}{2} \\ 0.2 \times \frac{t-3mT/2+\Delta T/2}{\Delta T} + 5.2 & \frac{3mT-\Delta T}{2} \leq t \leq \frac{3mT+\Delta T}{2} \end{cases}, \quad m = 1, 2, 3, \dots, \quad (\text{S49})$$

where  $T = 0.2$  s and  $\Delta T = 0.02$  s. The smooth step function of the resistor in Fig. 7b of the main text is

$$R_1(t) = \begin{cases} 5.2 & 0 \leq t \leq \frac{2T-\Delta T}{2} \\ 0.2 \times \frac{t-T+\Delta T/2}{\Delta T} + 5.2 & \frac{T-\Delta T}{2} \leq t \leq \frac{2T+\Delta T}{2} \\ 5.4 & \frac{2T+\Delta T}{2} \leq t \leq \frac{3T-\Delta T}{2} \\ -0.08 \times \frac{t-3T+\Delta T/2}{\Delta T} + 5.4 & \frac{3T-\Delta T}{2} \leq t \leq 2T + \frac{\Delta T}{2} \\ 5.32 & 2T + \frac{\Delta T}{2} \leq t \leq \frac{5T}{2} - \frac{\Delta T}{2} \\ -0.12 \times \frac{t-5T/2+\Delta T/2}{\Delta T} + 5.32 & \frac{5T-\Delta T}{2} \leq t \leq \frac{5T+\Delta T}{2} \\ 5.2 & \frac{5T-\Delta T}{2} \leq t \leq 3T \end{cases}, \quad (\text{S50})$$

where  $T = 0.2$  s and  $\Delta T = 0.02$  s.

- 
- [1] Yangyang Chen, Gengkai Hu, and Guoliang Huang. A hybrid elastic metamaterial with negative mass density and tunable bending stiffness. *Journal of the Mechanics and Physics of Solids*, 105:179–198, 2017.
  - [2] H Nassar, H Chen, AN Norris, and GL Huang. Quantization of band tilting in modulated phononic crystals. *Physical Review B*, 97(1):014305, 2018.
  - [3] Shaoyun Wang, Zhou Hu, Qian Wu, Hui Chen, Emil Prodan, Rui Zhu, and Guoliang Huang. Smart patterning for topological pumping of elastic surface waves. *Science Advances*, 9(30):eadh4310, 2023.
  - [4] Max Born and Emil Wolf. *Principles of optics: electromagnetic theory of propagation, interference and diffraction of light*. Elsevier, 2013.
  - [5] Jie Ren. From elastic spin to phonon spin: symmetry and fundamental relations. *Chinese Physics Letters*, 39(12):126301, 2022.
  - [6] Michael E Peskin. *An introduction to quantum field theory*. CRC press, 2018.
  - [7] Anthony Zee. *Quantum field theory in a nutshell*, volume 7. Princeton university press, 2010.
  - [8] Tom Lancaster and Stephen J Blundell. *Quantum field theory for the gifted amateur*. OUP Oxford, 2014.
  - [9] Singiresu S Rao. *Vibration of continuous systems*. John Wiley & Sons, 2019.
  - [10] Cornelius Lanczos. *The variational principles of mechanics*. Courier Corporation, 2012.